

Production of π^0 and η mesons at large transverse momenta in pp and $p\text{Be}$ interactions at 530 and 800 GeV/c

L. Apanasevich,^{4,9} J. Bacigalupi,¹ W. Baker,³ M. Begel,⁹ S. Blusk,⁸ C. Bromberg,⁴ P. Chang,⁵ B. Choudhary,² W. H. Chung,⁸ L. de Barbaro,⁹ W. DeSoi,⁹ W. Długosz,⁵ J. Dunlea,⁹ E. Engels, Jr.,⁸ G. Fanourakis,⁹ T. Ferbel,⁹ J. Ftacnik,⁹ D. Garelick,⁵ G. Ginther,⁹ M. Glaubman,⁵ P. Gutierrez,⁶ K. Hartman,⁷ J. Huston,⁴ C. Johnstone,³ V. Kapoor,² J. Kuehler,⁶ C. Lirakis,⁵ F. Lobkowicz,^{9,*} P. Lukens,³ J. Mansour,⁹ A. Maul,⁴ R. Miller,⁴ B. Y. Oh,⁷ G. Osborne,⁹ D. Pellett,¹ E. Prebys,⁹ R. Roser,⁹ P. Shepard,⁸ R. Shivpuri,² D. Skow,³ P. Slattery,⁹ L. Sorrell,⁴ D. Striley,⁵ W. Toothacker,^{7,*} S. M. Tripathi,¹ N. Varelas,⁹ D. Weerasundara,⁸ J. J. Whitmore,⁷ T. Yasuda,⁵ C. Yosef,⁴ M. Zielinski,⁹ and V. Zutshi²

(Fermilab E706 Collaboration)

¹University of California-Davis, Davis, California 95616, USA

²University of Delhi, Delhi, India 110007

³Fermi National Accelerator Laboratory, Batavia, Illinois 60510, USA

⁴Michigan State University, East Lansing, Michigan 48824, USA

⁵Northeastern University, Boston, Massachusetts 02115, USA

⁶University of Oklahoma, Norman, Oklahoma 73019, USA

⁷Pennsylvania State University, University Park, Pennsylvania 16802, USA

⁸University of Pittsburgh, Pittsburgh, Pennsylvania 15260, USA

⁹University of Rochester, Rochester, New York 14627, USA

(Received 24 April 2002; revised manuscript received 28 May 2003; published 11 September 2003)

We present measurements of the production of high transverse momentum π^0 and η mesons in pp and $p\text{Be}$ interactions at 530 and 800 GeV/c. The data span the kinematic ranges: $1 < p_T < 10$ GeV/c in transverse momentum and 1.5 units in rapidity. The inclusive π^0 cross sections are compared with next-to-leading order QCD calculations and to expectations based on a phenomenological parton- k_T model.

DOI: 10.1103/PhysRevD.68.052001

PACS number(s): 12.38.Qk, 13.85.Ni

I. INTRODUCTION

The study of inclusive single-hadron production at large transverse momentum (p_T) has been a useful probe in the development of perturbative quantum chromodynamics (PQCD) [1,2]. Early in the evolution of the parton model, a departure from an exponential dependence of particle production at lower p_T was interpreted in terms of the onset of interactions between pointlike constituents (partons) contained in hadrons. Perturbative methods have been applied to QCD at large p_T to provide quantitative comparisons with data. Such comparisons yield information on the validity of the PQCD description, and on parton distribution functions of hadrons and fragmentation functions of partons.

This paper reports high-precision measurements of the production of π^0 and η mesons with large p_T . The π^0 production cross sections are compared with next-to-leading order (NLO) PQCD calculations [3]. As illustrated in a previous publication [4], our data, for both inclusive π^0 and direct-photon production, are not described satisfactorily by the available NLO PQCD calculations, using standard choices of parameters. Similar discrepancies have been observed [5,6] between conventional PQCD calculations and other measurements of π^0 and direct-photon cross sections at large p_T (see also [7–9]). The origin of these discrepancies can be attributed to effects of initial-state soft-gluon radiation. Such radiation generates transverse components of

initial-state parton momenta, referred to below as k_T [10]. Evidence of significant k_T in various processes, and a phenomenological model for incorporating its effect on high- p_T cross sections, have been discussed extensively in Ref. [5]; recent studies of photoproduction of direct photons at HERA may provide additional insights [11–15]. The inadequacy of NLO PQCD in describing k_T -sensitive distributions has been discussed in Ref. [16]. In this paper, we follow the phenomenological prescription of Ref. [5] in comparing calculations with our π^0 data. We also present cross sections for η meson production at large- p_T . As might have been expected from previous measurements (see, e.g., [17]), η relative to π^0 production shows little dependence on p_T or on center of mass rapidity (y_{cm}).

II. THE EXPERIMENTAL SETUP

The E706 experiment at Fermilab was designed to measure direct-photon production at high- p_T , and to investigate the structure of events containing direct photons. The data collection phase of the experiment spanned three fixed-target running periods, and included a relatively low statistics commissioning run in 1987–88 [17–20], and primary data runs in 1990 and 1991–92. The results presented here are from data recorded during the 1991–92 run. The E706 apparatus, operated in tandem with the E672 muon spectrometer, constituted the “Meson West Spectrometer,” displayed schematically in Fig. 1. The experiment used a right-handed Cartesian coordinate system, with the Z-axis pointed in the nominal beam direction, and the Y-axis pointed upward. The principal elements of the Meson West Spectrometer are discussed below.

*Deceased.

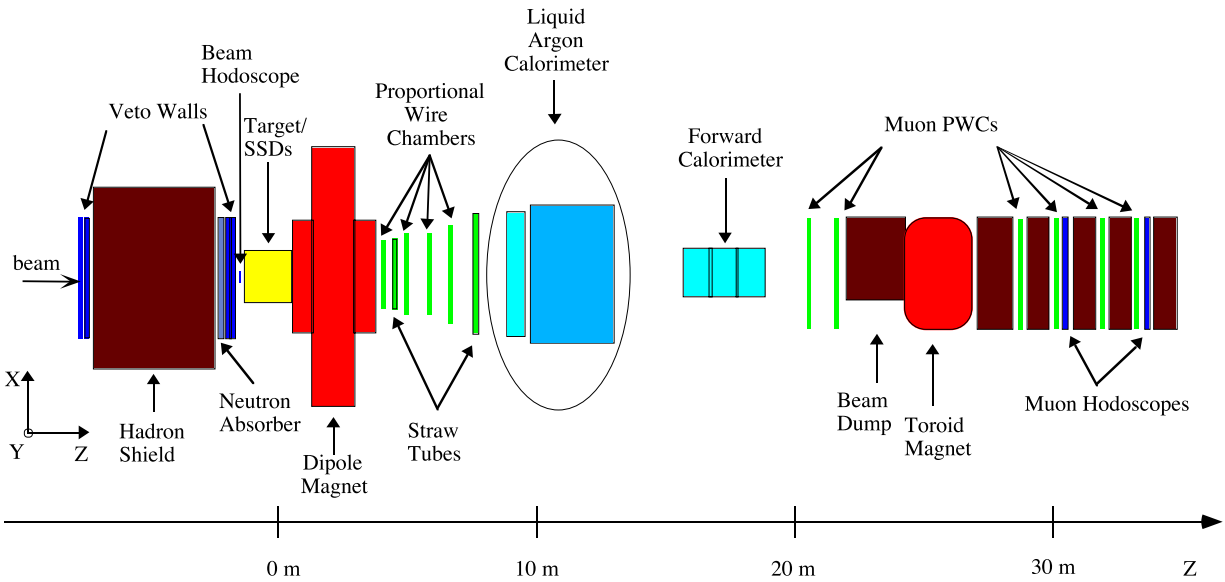


FIG. 1. Plan view of the Fermilab Meson West spectrometer, as configured for the 1991-92 fixed target run.

A. Beamline and target

The Meson West beamline was capable of transporting either 800 GeV/c primary protons from the Fermilab Tevatron or secondary beams of either polarity. We report here on results from studies using 800 GeV/c primary protons and a 530 GeV/c positive secondary beam. The beamline was instrumented with a differential Cherenkov counter [21,22] to identify incident pions, kaons, and protons in secondary beams. This helium-filled counter was 43.4 m long and was located ≈ 100 m upstream of the experiment’s target. The proton fraction at 530 GeV/c was determined via the Cherenkov counter to be 97% [21].

A 4.7 m long stack of steel surrounding the beam pipe was placed between the last beamline magnet and the target box (see Fig. 1) to absorb hadrons. A water tank was placed at the downstream end of this hadron shield to absorb low-energy neutrons. During the 1991-92 run, two walls of scintillation counters were located both upstream and downstream of the hadron shield, which were used to identify penetrating muons.

The target region during the 1991-92 run consisted of two 0.8 mm thick copper disks of 2.5 cm diameter, located immediately upstream of a liquid hydrogen target, followed by a 2.54 cm long beryllium cylinder, 2.54 cm in diameter. The hydrogen target consisted of a 15 cm long mylar flask, supported in an evacuated volume, with beryllium windows at each end (2.5 mm thickness upstream and 2.8 mm thickness downstream) [23].

B. Charged-particle tracking

The spectrometer employed a charged-particle tracking system consisting of silicon strip detectors (SSDs) [24], a dipole analysis magnet, proportional wire chambers (PWCs), and straw-tube drift chambers (STDCs) [25]. The SSD system consisted of 16 planes of silicon wafers, arranged in eight modules. Each module contained two SSD planes, providing information along the horizontal (X) and vertical

(Y) directions. Six 3×3 cm² SSD planes were located upstream of the target and used to reconstruct beam tracks. Two hybrid 5×5 cm² SSD planes were located ≈ 2 cm downstream of the Be target [26]. These planes had 25 μ m pitch strips in the central 1 cm, and 50 μ m pitch strips beyond. They were followed by eight 5×5 cm² SSD planes of 50 μ m pitch. The SSDs were instrumented to cover a solid angle of ± 125 mr. Figure 2 displays the reconstructed vertex position as a function of Z for a representative sample of 1991-92 data, showing clear separation of the different target elements.

The analysis dipole magnet imparted a transverse momentum impulse of ≈ 450 MeV/c in the horizontal plane to singly charged particles. Downstream track segments were measured by means of four stations of four views ($XYUV$) [27] of 2.54 mm pitch PWCs and two stations of eight ($4X4Y$) layers of STDCs with tube diameters 1.03 cm for the upstream station, and 1.59 cm for the downstream station. The STDC stations were installed prior to the 1990 fixed-target run, and improved the angular resolution of the downstream tracking system (to ≈ 0.06 mrad) to make it comparable to that of the upstream system.

C. Calorimetry

The central element of the E706 apparatus was a finely segmented liquid argon electromagnetic calorimeter (EMLAC) used to detect and measure electromagnetic showers [28,29]. The EMLAC had cylindrical geometry, with an inner radius of 20 cm and an outer radius of 160 cm. It was divided into four mechanically independent quadrants, which were further subdivided electronically to create octants. The calorimeter had 33 longitudinal cells read out in two sections: an 11 cell front section, comprising ≈ 8.5 radiation lengths, and a 22 cell back section, comprising ≈ 18 radiation lengths. This front/back split was used for measuring the direction of incidence of showering particles, for discriminating between electromagnetic and hadronic showers, and

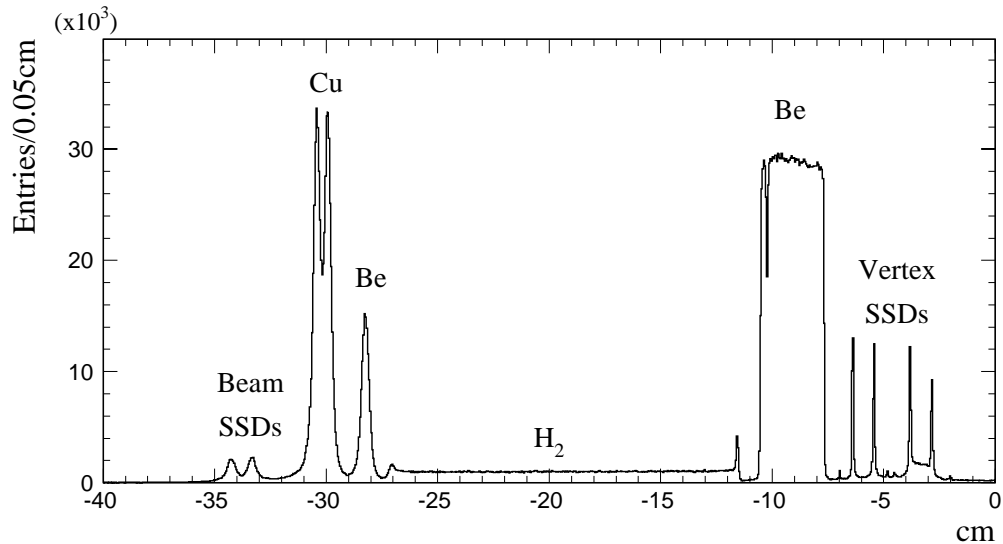


FIG. 2. Distribution of the reconstructed vertex position (along the beam axis) for the combined 530 and 800 GeV/c data. The clearly resolved individual target elements are, from the left: two copper foils, the liquid hydrogen target (a mylar flask enclosed between two thin Be windows), followed by the main beryllium target. The two silicon strip detectors (SSDs) immediately upstream and four downstream of the target can also be easily distinguished.

for resolving closely separated electromagnetic showers. The longitudinal cells consisted of 2 mm thick lead cathodes (the first cathode was constructed of aluminum), double-sided copper-clad G-10 radial (R) anode boards, followed by 2 mm thick lead cathodes and double-sided copper-clad G-10 azimuthal (Φ) anode boards. There were 2.5 mm argon gaps between each of these layers in a cell. The physical layout is illustrated in Fig. 3.

The copper-cladding on the anode boards was cut to form strips. Signals from corresponding strips from all R (or Φ) anode boards in the front (or back) section were jumpered together. The copper-cladding on the radial anode boards was cut into concentric strips centered on the nominal beam axis.

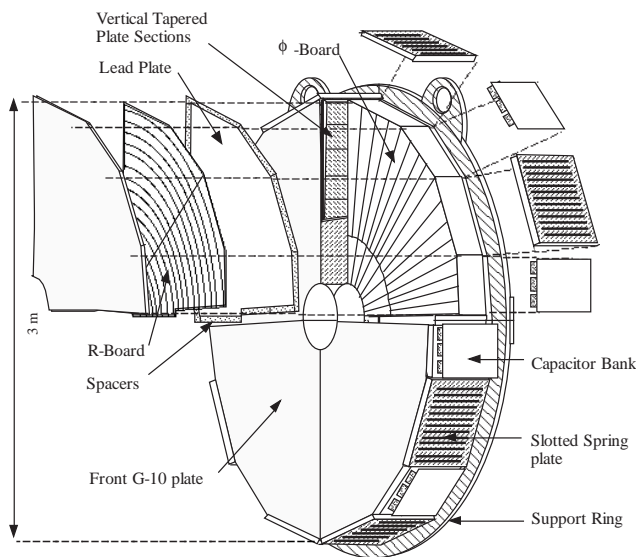


FIG. 3. The physical layout of the electromagnetic liquid argon calorimeter (EMLAC).

The width of the strips on the first R board was 5.5 mm. The width of the R strips on the following R boards increased slightly so that the radial geometry was projective relative to the target, which was located 9 m upstream of the EMLAC. The azimuthal readout was subdivided at a radius of 40 cm into inner and outer segments, with each inner Φ strip subtending an azimuthal angle of $\pi/192$ radians, and outer Φ strips covering $\pi/384$ radians. Subdivision of the azimuthal strips in the outer portion of the detector improved both the position and energy resolution for showers reconstructed in this region. It also reduced $R-\Phi$ correlation ambiguities from multiple showers in the same octant of the calorimeter.

Data acquisition and trigger-signal processing for the EMLAC was based upon the FNAL RABBIT system [30]. The zero suppression features of this system were used extensively during the experiment's 1987-88 commissioning run to achieve tolerable deadtimes. However, zero suppression limited our ability to quantify the effects of out-of-time photon-induced showers and the tails of hadron-induced showers, thereby compromising efforts to characterize the detailed response of the detector. Consequently, FASTBUS modules [the ICBM (Intelligent Control and Buffering Module) and the Wolf interface [31,32]] were developed by E706 to replace the original, CDF-designed, MX readout controllers. These FASTBUS modules enabled us to read in all channels and therefore eliminate zero suppression during the experiment's two primary data runs.

The apparatus also included two other calorimeters: a hadronic calorimeter (HALAC) located downstream of the EMLAC in the same cryostat, and a steel and scintillator calorimeter (FCAL), positioned further downstream, to increase coverage in the very forward region. The HALAC had 53 longitudinal cells read out in 2 sections: a 14 cell front section, comprising ≈ 2 interaction lengths, and a 39 cell back section, comprising ≈ 6 interaction lengths. Each cell

consisted of read-out planes separated by 3 mm argon gaps and a 2.5 cm thick steel plate.

The FCAL acceptance covered the beam hole region of the EMLAC. It was split into three longitudinally similar sections. Each section was composed of alternating layers of 1.9 cm thick steel absorber plates and 4.8 mm thick acrylic scintillator sheets. The distance between steel plates was 6.9 mm. The downstream module contained 32 steel absorber plates and 33 scintillator sheets; the other two modules were comprised of 28 steel absorber plates and 29 scintillator sheets. Together, the three modules constituted ≈ 10.5 interaction lengths of material.

D. Muon identification

The E672 muon spectrometer, consisting of a toroidal magnet, shielding, scintillators, and proportional wire chambers, was deployed immediately downstream of the FCAL. The combined Meson West Spectrometer was triggered on high-mass muon pairs in order to investigate the hadroproduction of J/ψ , $\psi(2s)$, χ_c , and B mesons [33–36]. E706 and E672 collected data simultaneously and shared trigger logic, the data acquisition system, and event reconstruction programs. Data collected with the dimuon trigger were also used for several technical studies, for example, the $J/\psi \rightarrow \mu^+ \mu^-$ signal was used to calibrate the momentum scale of the tracking system.

E. Triggering

The E706 trigger selected interactions yielding high transverse momentum showers in the EMLAC [37]. The selection process involved four stages: beam and interaction definitions, pretrigger requirements, and the final trigger requirements. Beam particles were detected using a hodoscope consisting of three planes (arranged in X , Y and U views) of scintillator, located ≈ 2 m upstream of the target region. Each plane contained 12 scintillator strips. The widths of the strips transverse to the beam direction varied from 1 mm in the central region to 5 mm along the edges. The edges of individual strips in each plane were overlapped to avoid gaps in acceptance. A BEAM signal was generated by a coincidence of signals from counters in at least two of the three hodoscope planes. The BEAM1 signal required that less than two hodoscope planes detected two or more isolated clusters of hits in coincidence with BEAM. This BEAM1 requirement rejected events with multiple beam particles incident upon the target. A plane of four scintillation counters, referred to as beam hole counters, arranged to produce a 0.95 cm diameter central hole was located downstream of the beam hodoscope and used to reject interactions initiated by particles in the beam halo.

Two pairs of scintillation counters were mounted on the dipole analysis magnet, one pair upstream and the other downstream of the magnet. Each pair had a central hole that allowed noninteracting beam particles to pass through undetected. An INTERACTION was defined as a coincidence between signals from at least two of these four interaction counters. A filter was used to reject interactions that occurred within 60 ns of one other to minimize potential confusion in

the EMLAC due to out-of-time interactions.

For those interactions that satisfied both the BEAM1 and INTERACTION definitions, the p_T deposited in various regions of the EMLAC was evaluated by weighting the energy signals from the fast outputs of the EMLAC R -channel amplifiers by $\approx \sin \theta_i$, where θ_i is the polar angle that the i th strip subtends relative to the nominal beam axis. The PRETRIGGER HI requirement was satisfied when the p_T detected either in the inner 128 R channels or the outer R channels of any octant was greater than the threshold value of ≈ 2 GeV/ c . A pretrigger signal was issued only if the signals from a given octant satisfied the pretrigger requirement, there was no evidence in that octant of substantial noise or significant p_T attributable to an earlier interaction, and there was no incident beam halo muon detected by the walls of scintillation counters surrounding the hadron shield upstream of the spectrometer. The pretrigger signal latched data from the various subsystems until a final trigger decision was made.

Localized trigger groups were formed for each octant by clustering the R channels into 32 groups of 8 channels. Each of the adjacent pairs of 8 channel groups (groups 1 and 2, 2 and 3, . . . , 31 and 32) formed a LOCAL group of 16 strips. If the p_T detected in any of these groups of 16 was above a specified high (or low) threshold, then a LOCAL HI (or LOCAL LO) signal was generated for that octant. The SINGLE LOCAL HI (SINGLE LOCAL LO) trigger required a LOCAL HI (LOCAL LO) signal from an octant that also satisfied the PRETRIGGER HI. The LOCAL HI (LOCAL LO) threshold was ≈ 3.5 GeV/ c (≈ 2 GeV/ c). The SINGLE LOCAL LO trigger was prescaled by a factor of ≈ 200 .

In addition to these high- p_T triggers, prescaled samples of low-bias BEAM, INTERACTION, and pretrigger events were also recorded. The prescale factors for these triggers were typically set at 15^6 , 15^5 , and 15^3 , respectively. These low-bias triggers constituted $\approx 10\%$ of the events recorded.

III. π^0 AND η ANALYSIS

The data sample used in this analysis corresponds to an integrated luminosity of 6.8 (1.1) events/pb for 530 GeV/ c p Be (pp) interactions, and 6.5 (1.1) events/pb at 800 GeV/ c . The following sections describe the analysis procedures and methods used to correct the data for losses resulting from inefficiencies and selection biases.

A. Event reconstruction

The charged-track reconstruction algorithm produced track segments upstream of the dipole magnet using information from the SSDs, and downstream of the magnet using information from the PWCs and STDCs. These track segments were projected to the center of the magnet, and linked to form the final tracks and the interaction vertex. The charged-track reconstruction and vertex-finding methodology are described in Ref. [37].

The readout in each EMLAC quadrant consisted of four regions: left R and right R (radial strips of each octant in that quadrant), and inner Φ and outer Φ regions (azimuthal strips divided at $R=40$ cm). Strip energies from clusters in each

region were fitted to the shape of electromagnetic showers, as determined from Monte Carlo simulations and isolated-shower data. These fits were used to evaluate the positions and energies (E_R and E_Φ) of the peaks in each region. Shower positions and energies were obtained by correlating peaks of approximately the same energy in the R and Φ regions within the same half octant; more complex algorithms were used to handle configurations with overlapping showers in either the R or Φ regions. Any differences in photon energy measured in the R and Φ views reflect the intrinsic resolution properties of the calorimeter, and provide a test of the quality of the Monte Carlo simulations. The EMLAC's longitudinal segmentation provided discrimination between showers generated by electromagnetically or hadronically interacting particles. For individual showers, the ratio of energy reconstructed in the front section to the sum of energy in the front and back section of the EMLAC, referred to as $E_{\text{FRONT}}/E_{\text{TOTAL}}$, also tested the Monte Carlo simulation of longitudinal shower development (see the detector simulation section below). An expanded discussion of the EMLAC reconstruction procedures and performance can be found in Ref. [29].

B. Data sample selection and corrections

Events contributing to measurements of cross sections were required to have reconstructed vertices within the fiducial volume of the Be or H_2 targets. Vertex reconstruction efficiencies were evaluated for each target using a detailed Monte Carlo simulation of the spectrometer, as described below. These efficiencies were used to correct reconstruction losses and resolution smearing across fiducial boundaries of the targets. The vertex reconstruction efficiency was ≈ 1 for the H_2 and downstream Be targets, and 0.97 for the upstream Be target.

Both π^0 and η mesons were reconstructed via their $\gamma\gamma$ decay modes. The photons were required to be within the fiducial region of the EMLAC, which excluded areas with reduced sensitivity. In particular, photons incident upon regions of the detector near quadrant boundaries (which abutted steel support plates), the central beam hole, the outer radius of the EMLAC, and octant boundaries were excluded from consideration. In addition, $\gamma\gamma$ combinations were considered as π^0 or η candidates only when the two photons were detected in the same octant, to simplify subsequent analysis of the trigger response. A simple ray-tracing Monte Carlo program was employed to determine the correction for losses to signal incurred from the application of these fiducial requirements. Simulated π^0 and η mesons were allowed to decay isotropically to two photons and were binned in p_T , rapidity, and vertex position. Photon pairs that satisfied the energy asymmetry requirement were projected to the EMLAC, and selected on the basis of the fiducial acceptance criteria.

Only showers with at least 20% of their shower energy deposited in the front part of EMLAC, $E_{\text{FRONT}}/E_{\text{TOTAL}} > 0.2$, were accepted as photon candidates to reduce the background from hadrons. A full simulation of the showers in the calorimeter was employed to correct cross sections for

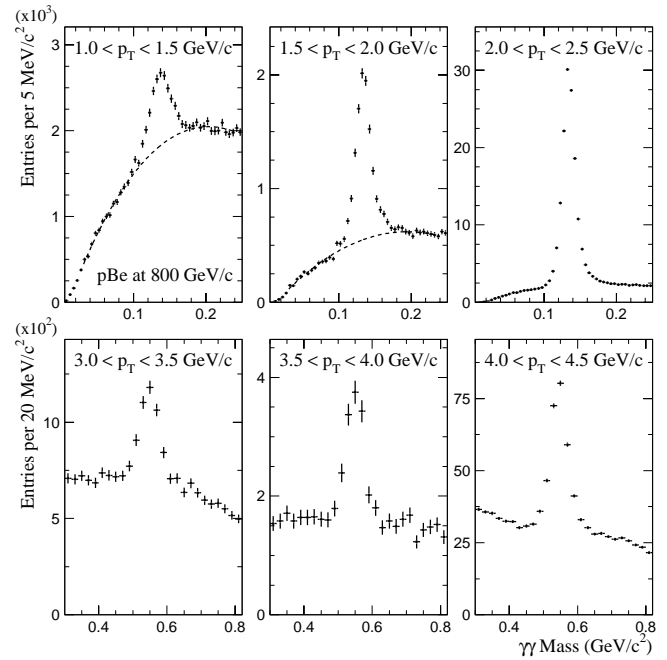


FIG. 4. $\gamma\gamma$ mass distributions in the region of the π^0 (top row) and the η (bottom row) mesons from $p\text{Be}$ interactions at 800 GeV/c, for several ranges of $\gamma\gamma$ p_T -values. Curves are overlaid for those p_T bins where background to signal was determined using a fitting procedure rather than sideband subtraction.

this requirement, as well as for other larger effects including resolution-smearing and reconstruction losses. Only $\gamma\gamma$ combinations with energy asymmetry [$A_{\gamma\gamma} \equiv |E_{\gamma_1} - E_{\gamma_2}| / (E_{\gamma_1} + E_{\gamma_2})$] less than 0.75 were considered, to reduce uncertainties due to low energy photons.

Invariant mass distributions in the π^0 and η regions for photon pairs that satisfied the above requirements are shown in Fig. 4 for representative low- p_T intervals. A π^0 candidate was defined as a combination of two photons, originating at the reconstructed interaction vertex, with invariant mass $M_{\gamma\gamma}$ in the range $100 \text{ MeV}/c^2 < M_{\gamma\gamma} < 180 \text{ MeV}/c^2$. An η candidate was defined similarly as a two-photon combination in the range $450 \text{ MeV}/c^2 < M_{\gamma\gamma} < 650 \text{ MeV}/c^2$. To obtain production cross sections, combinatorial background in the π^0 and η regions was evaluated as follows. Using the same acceptance criteria as for the peak regions, sideband regions were defined to cover an equivalent mass range of the π^0 and η peak regions. The p_T and rapidity distributions from these side bands were then subtracted from the corresponding distributions within the π^0 and η mass ranges to obtain the respective signals. This technique is appropriate as long as the combinatorial background depends approximately linearly on $M_{\gamma\gamma}$. At p_T below $\approx 2 \text{ GeV}/c$, the shape of the combinatorial background in the signal regions is not linear, and a more sophisticated fitting procedure was used to evaluate the background. The $\gamma\gamma$ mass distributions were fitted using Gaussians for signal and second and third-order polynomials in $M_{\gamma\gamma}$ to represent the background. Several fits were carried out for each distribution and then averaged to determine the combinatorial background in the peak regions. The signals were defined as the differences between the to-

tals and the averaged backgrounds.

The signals were corrected for losses due to the requirement on energy asymmetry and for branching fractions [38] into $\gamma\gamma$ decay modes. The correction for losses from the conversion of one or both of the photons into e^+e^- pairs was evaluated by projecting each reconstructed photon from the event vertex to the reconstructed position in the EMLAC. The number of radiation lengths of material traversed along the photon path was calculated on the basis of a detailed description of the detector, and the photon conversion probability evaluated, and used to account for losses from conversion.

C. Trigger response

As mentioned previously, the SINGLE LOCAL HI and SINGLE LOCAL LO trigger decisions were based upon depositions of p_T in the EMLAC within groups of 16 contiguous radial strips. The efficiency of each trigger group of 16 was evaluated as a function of the p_T reconstructed within the group, using data samples that were not biased in that region. The sample used for obtaining the efficiency of the SINGLE LOCAL HI trigger was based on information from octants that fired the SINGLE LOCAL LO trigger. The sample used to evaluate the response of the SINGLE LOCAL LO trigger used information from the octants opposite those that satisfied the SINGLE LOCAL HI trigger. In the case of the PRETRIGGER HI, octants located opposite those that satisfied the SINGLE LOCAL HI trigger were used to measure the trigger efficiency for the trigger groups comprised of the inner and outer R channels in each octant.

A probability to satisfy the trigger was defined for each π^0 or η candidate based upon the energy deposition in the entire octant, $P = 1 - \prod(1 - p_i)$, where p_i is the efficiency of the i th trigger group in the octant containing the candidate. The inverse of this probability was applied as a trigger weight to each meson candidate. Meson candidates with trigger probabilities of $P < 0.1$ were excluded from further consideration to avoid excessively large trigger weights. The correction for losses from this requirement was determined from Monte Carlo, and absorbed into the reconstruction efficiency.

The cross sections presented in this paper combine results from the INTERACTION, PRETRIGGER HI, SINGLE LOCAL LO, and SINGLE LOCAL HI triggers. The p_T spectra, corrected only for prescale factors, from a representative sample of these triggers are shown in Fig. 5. The transition points chosen between the high and low threshold triggers were determined by comparing the fully corrected results from each trigger, and were different for π^0 and η mesons, and also depended on rapidity. Additional details on the trigger can be found in Refs. [37,39,40].

D. Rejection of beam halo muons

Spurious triggers were produced by muons in the beam halo that deposited energy in the electromagnetic calorimeter in random coincidence with an interaction in the target. Particularly in the outer regions of the EMLAC, such energy depositions can satisfy the high- p_T LOCAL trigger require-

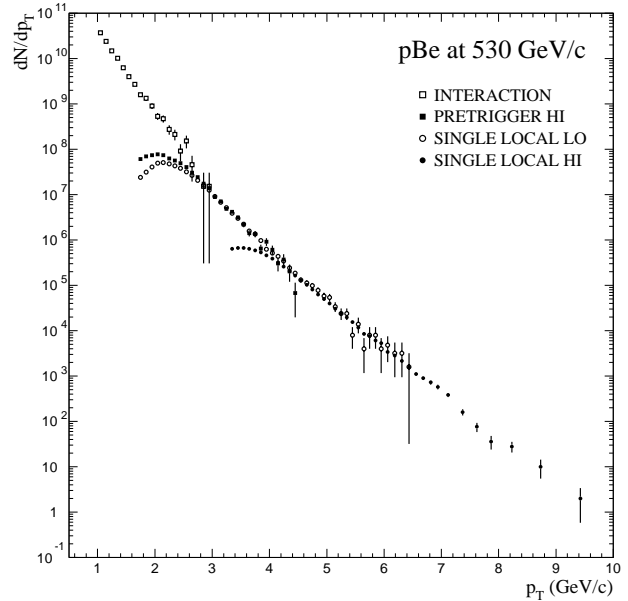


FIG. 5. p_T spectra of π^0 candidates from 530 GeV/c proton interactions on Be, selected via several different triggers and implemented with significantly different prescale factors. The data have been corrected only for trigger prescale factors.

ments. This occurred much more frequently in data from the 530 GeV/c secondary beam than for the primary 800 GeV/c beam because of the presence of an upstream interaction target in the former case. To reduce this background, the pre-trigger logic relied on signals from the veto walls of scintillator counters to reject events associated with such muons in the beam halo. In the off-line analysis, we employed expanded requirements on the latched veto-wall signals, the direction of reconstructed showers [29], the shower shape (such muon-induced showers have a different shape than electromagnetic showers that originate from the interaction vertex), and the total p_T imbalance in the event. For the latter, we calculated the net p_T of the photons and charged particles which, based upon their initial trajectories, would have intercepted the EMLAC in the transverse plane within the 120° sector opposite the meson candidate (P_T^{away}). In interactions that generate a high- p_T meson, the ratio of P_T^{away} to the p_T of the meson should be near unity. However, for events triggered by showers from muons in the beam halo, P_T^{away}/p_T should be very small, since the interaction in random coincidence with the muon is typically a soft interaction. Candidates with $P_T^{away}/p_T < 0.3$ were considered likely to be due to muons from the beam halo and were rejected.

To illustrate the effect of the above off-line requirements, $\gamma\gamma$ invariant mass distributions, both before and after application of the rejection criteria, are shown in Fig. 6 for the 530 and 800 GeV/c data, for $\gamma\gamma$ pairs with $p_T > 7.0$ GeV/c. The large muon-induced background at low $\gamma\gamma$ mass values in the 530 GeV/c data is due to the occasional splitting of the muon-induced showers into two closely separated photon candidates. This happens because the reconstruction software assumes that the showers origi-

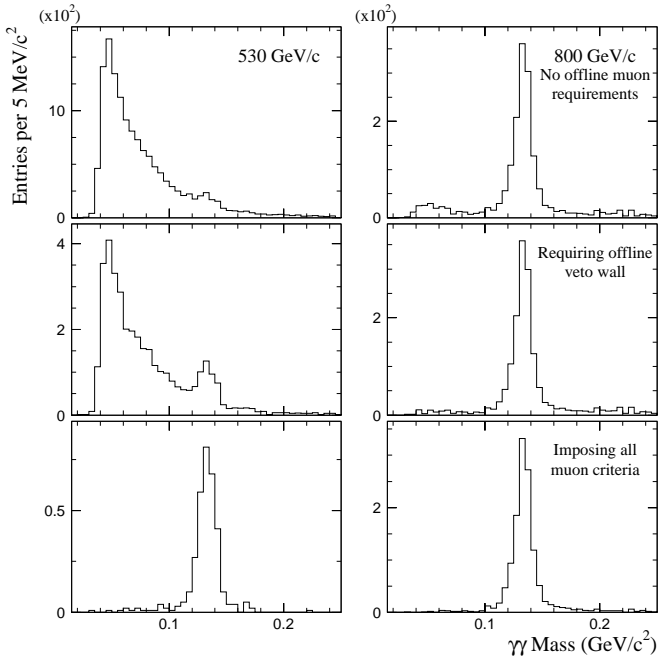


FIG. 6. Effect of muon discrimination on the invariant mass distribution in the π^0 -mass region, for candidate $\gamma\gamma$ pairs with $p_T > 7$ GeV/c in the 530 GeV/c data (left) and in the 800 GeV/c data (right).

nate from the target region rather than from the beam halo. The 800 GeV/c data have very few muon-induced triggers, and is consequently not affected very strongly by these rejection criteria.

The impact of these rejection criteria on signal was checked using more restrictive selection criteria to define a pure sample of $\gamma\gamma$ pairs. The fraction of signal lost by the application of each of the muon-rejection requirements was used to determine a correction to the cross section. The product of the correction factors for muon rejection corresponds to an increase of $\approx 8\%$ in the observed cross section at $p_T = 4$ GeV/c, and $\approx 10\%$ at $p_T = 7$ GeV/c, for the 530 GeV/c beam data. The corrections were much smaller for the 800 GeV/c data because of the lower muon content.

E. Detector simulation

The Meson West spectrometer was modeled using a detailed GEANT [41] simulation. Because the full simulation of electromagnetic showers requires extensive computing time, we developed a hybrid approach using GEANT-tracking through the magnetic spectrometer and in the initial stages of shower development in the calorimeter. We used the standard GEANT algorithms for tracking particles with energies above 10 MeV, below which we relied on an empirical parametrization for the deposition of energy in the EMLAC [42]. This cutoff was selected to be at the point at which bremsstrahlung still dominates energy loss in lead, and led to significant improvement in processing speed. In doing this, we took advantage of the steady advances in computational power of the FNAL UNIX farms [43] to reach the desired level of statistical accuracy.

As inputs to the GEANT simulation, we employed single-particle distributions, reconstructed events from data, and two event generators: HERWIG [44] and PYTHIA [45]. For the analyses to be described, we chose HERWIG as the principal Monte Carlo event generator because it provided a better match to particle multiplicities in the data using just the default parameters. Over 5.5 million HERWIG events were passed through the GEANT simulation. We weighted the HERWIG π^0 and η spectra in p_T and rapidity to match our measured results, so that the corrections obtained from the Monte Carlo were based on distributions in the data rather than the generator.

The calibration of the energy response of the EMLAC was based on the reconstructed masses of π^0 mesons in the $\gamma\gamma$ decay mode [29]. The steeply falling p_T spectrum for π^0 production, combined with the calorimeter's resolution, produced a small offset ($\approx 1\%$) in mean reconstructed photon energies. Using the same calibration procedure in the simulated EMLAC as in the detector, we corrected this offset and minimized any potential biases in the calibration. We also employed the GEANT Monte Carlo simulation to evaluate the mean correction as a function of photon energy for energy deposited in the material upstream of the EMLAC. The impact of detector resolution on the energy scale and on the π^0 and η production spectra was incorporated in the overall reconstruction efficiency corrections.

To ensure that the Monte Carlo simulation reproduced the data, a special preprocessor was used to convert GEANT information into signals and strip energies as measured in the various detectors, and to simulate hardware effects, such as channel noise and gain variations. The generated Monte Carlo events were then processed through the same reconstruction software used for the analysis of data, and thereby provided measures of inefficiencies and biases for the reconstruction algorithms.

Comparisons between results from the Monte Carlo simulation and the data for the distributions in $E_R - E_\phi$ and $E_{\text{FRONT}}/E_{\text{TOTAL}}$ are presented in Figs. 7 and 8. The Monte Carlo results are in satisfactory agreement with the data, indicating that the simulation treats shower development in the EMLAC properly. Figures 9 and 10 show the $\gamma\gamma$ mass spectra in the π^0 and η mass regions for two minimum- p_T requirements, and compare these to the simulated spectra. In addition to giving further evidence that the Monte Carlo provides good simulation of the resolution of the EMLAC, the agreement in the levels of combinatorial background indicates that the Monte Carlo also provides reasonable simulation of the underlying event structure. Figure 11 shows a comparison between Monte Carlo and data for the sideband-subtracted energy asymmetry distribution ($A_{\gamma\gamma}$) for photons from π^0 decays. The agreement indicates that the Monte Carlo accurately describes the losses of low-energy photons.

Reconstruction efficiencies for π^0 and η mesons that satisfied the $A_{\gamma\gamma}$ and fiducial requirements were relatively high over most of the kinematic range. Figure 12 shows the probability for a π^0 to pass the selection requirements imposed on the Monte Carlo events at 530 GeV/c as a function of p_T , for different rapidity intervals. This probability includes losses due to the reconstruction algorithm, the

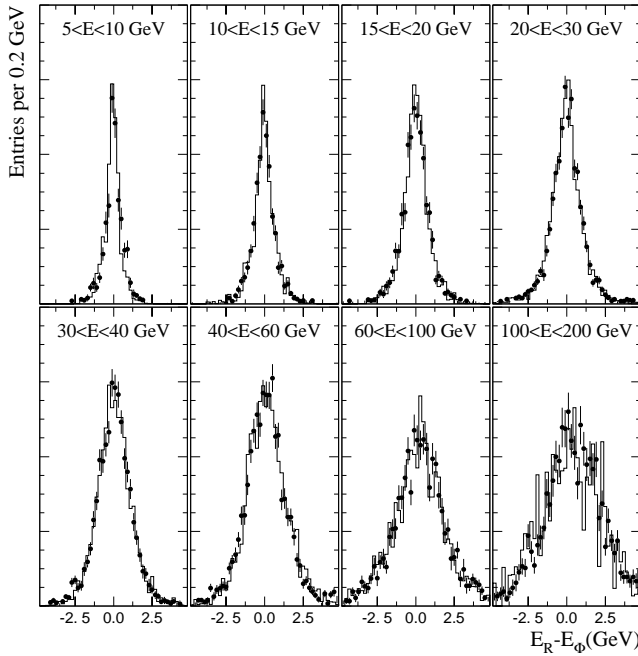


FIG. 7. Comparison of distributions in $E_R - E_\phi$ for photons in data (histogram) and Monte Carlo (points) from π^0 candidates with $p_T > 3.5$ GeV/c in the 530 GeV/c sample. The distributions are shown for various photon energy ranges and each has been normalized to unit area.

$E_{\text{FRONT}}/E_{\text{TOTAL}}$ requirement, and the 10% minimum trigger probability requirement. The drop in efficiency at forward rapidities and high p_T is attributable to the increased difficulty in separating the two photons from π^0 decays in this kinematic region.

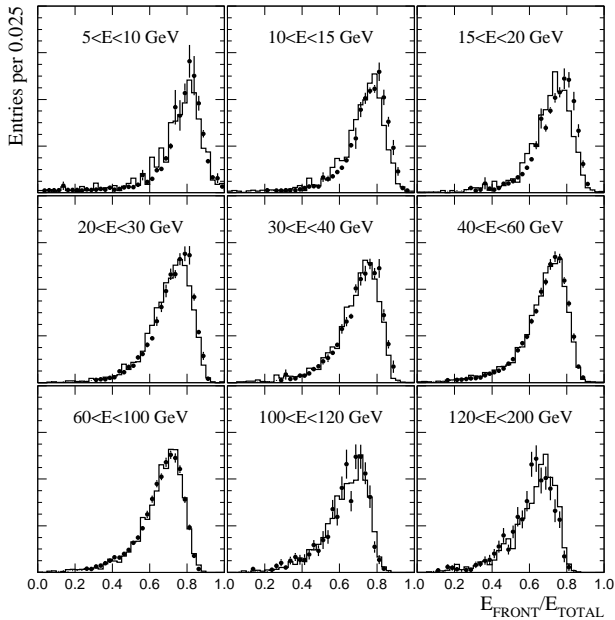


FIG. 8. Comparison of $E_{\text{FRONT}}/E_{\text{TOTAL}}$ distributions for photons in data (histogram) and Monte Carlo (points) from π^0 candidates with $p_T > 3.5$ GeV/c in the 800 GeV/c sample. The distributions are shown for various photon energy ranges and each has been normalized to unit area.

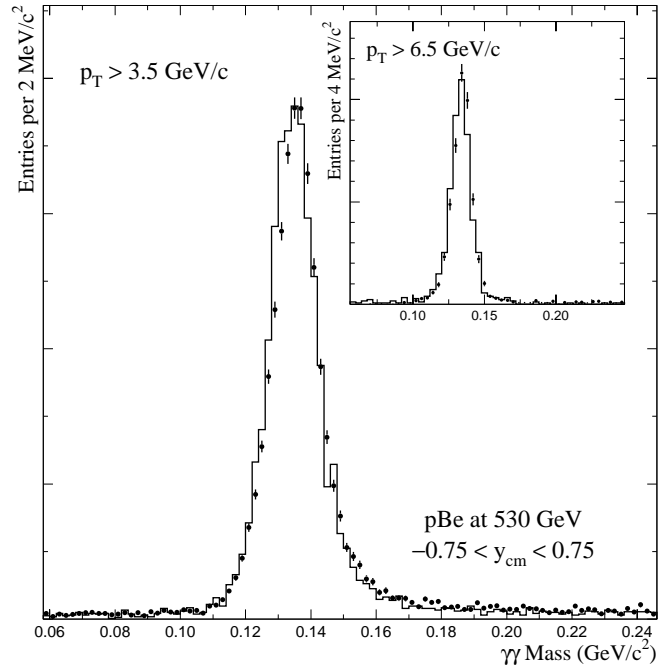


FIG. 9. $\gamma\gamma$ mass distributions in the π^0 signal region in 530 GeV/c data (histogram) compared to Monte Carlo (points) for two requirements on the minimum p_T of the photon pair. The distributions have been normalized to unit area.

F. Normalization

Electronic scalars that counted signals from the beam hodoscope, interaction counters, and beam hole counters were used to determine the number of beam particles incident on

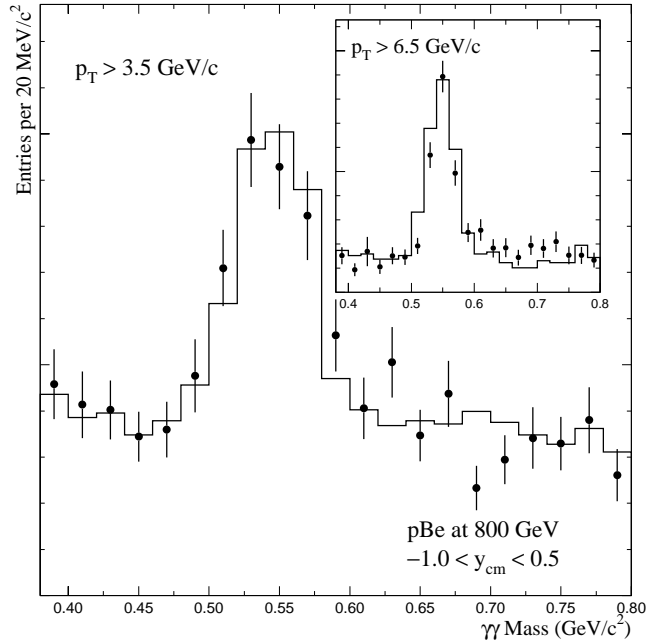


FIG. 10. $\gamma\gamma$ mass distributions in the η signal region in 800 GeV/c data (histogram) compared to Monte Carlo (points) for two requirements on the minimum p_T of the photon pair. The distributions have been normalized to unit area.

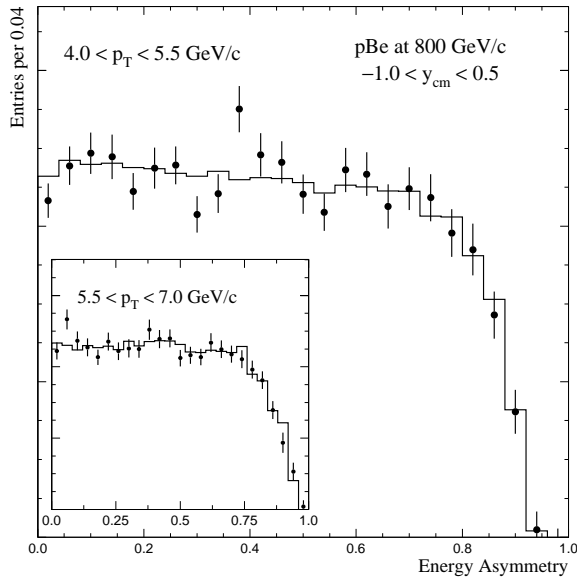


FIG. 11. Comparison of asymmetry in energy for photons from π^0 mesons in data (histogram) and Monte Carlo (points) for 800 GeV/c p Be interactions, for the π^0 p_T intervals $4.0 < p_T < 5.5$ GeV/c and $5.5 < p_T < 7.0$ GeV/c. These background-subtracted distributions have been normalized to unit area.

the target. Other scalers logged the state of the trigger and components of the data acquisition system. Information from these scalers was used to determine the number of beam particles that traversed the spectrometer when it was ready to record data. This was corrected for multiple occupancy in the beam hodoscope beyond that excluded via the

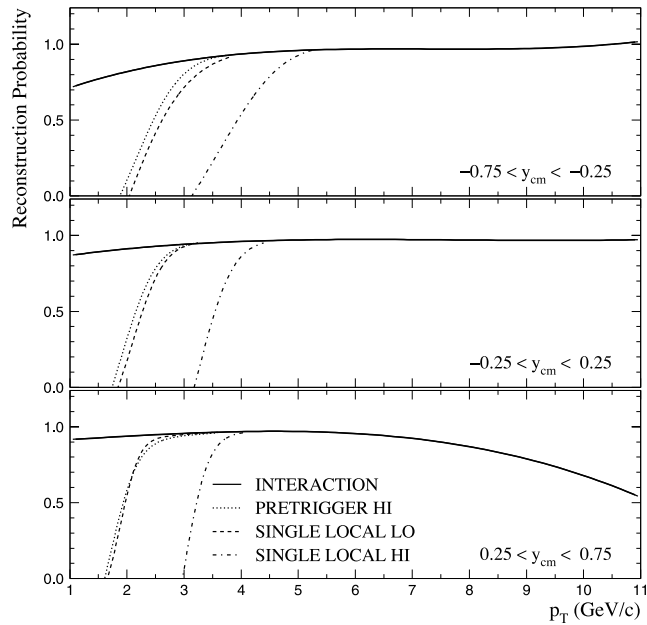


FIG. 12. Reconstruction probability for π^0 mesons in the 530 GeV/c Monte Carlo sample as a function of p_T for three rapidity intervals and different triggers. This probability reflects the losses due to the reconstruction algorithm, the $E_{\text{FRONT}}/E_{\text{TOTAL}}$ criterion, and the individual trigger requirements (see text for details).

BEAM1 requirement (Sec. II E) and for absorption of beam in target material.

The normalization of the π^0 cross section at low p_T was verified independently using events from the prescaled BEAM and INTERACTION trigger samples. For these samples, the absolute normalization can also be obtained by just counting events. The normalizations at low p_T , as determined from the scalers and via event counting techniques, were found to agree to 3% accuracy.

Based upon the good agreement between results from these independent normalization methods, combined with the stability of the results from different parts of the run, an evaluation of the internal consistency of the scalers, and a detailed analysis of the design, implementation and performance of the trigger, the net systematic uncertainty in overall normalization is estimated to be $\approx 8\%$.

G. Secondary beam contamination

The 530 GeV/c cross sections were corrected for the estimated small admixture of 2.75% π^+ and 0.5% K^+ in the beam [21]. Although the percentage contamination is small, its effect at high p_T is enhanced by the presence of two, rather than three, valence quarks in the incident mesons. The effect of incident π^+ contamination was estimated using our high-statistics study of π^0 and η meson production in 515 GeV/c π^- collisions [4]. This is justified because: (a) neutral-meson production by incident π^+ and π^- beams is expected to be similar from arguments based on isospin symmetry and previous measurements [46]; (b) the π^+ component of the nominally 530 GeV/c positive secondary beam also had a mean momentum of 515 GeV/c; and (c) the ratio of the measured π^0 cross section from our Cherenkov-tagged π^+ component of the positive secondary beam to the corresponding cross section from the 515 GeV/c π^- beam was consistent with unity at large p_T [21].

The effect of K^+ contamination was assumed to be half that of the π^+ contamination, consistent with previous measurements at lower energy [47], and with our own statistically limited data [21]. After correcting for beam contamination, the cross sections at 530 GeV/c were reduced by $\approx 2\%$ at low p_T and by $\approx 10\%$ at high p_T .

H. Summary of systematic uncertainties

The principal contributions to the systematic uncertainty in the cross sections arose from the following sources: calibration of photon energy response, π^0 and η reconstruction efficiency and detector-resolution unsmearing, the overall normalization, and, for 530 GeV/c data, beam contamination. The relative systematic uncertainty for π^0 production at 530 GeV/c is shown as a function of p_T in Fig. 13. Included in the figure are the contributions from the major sources of systematic uncertainty. Other sources of uncertainty which contribute at the 1 to 2% level include: background subtraction, beam halo muon rejection, geometric acceptance, photon conversions, trigger response, and vertex finding. The total systematic uncertainty is calculated by combining in quadrature all the individual uncertainties. The correspond-

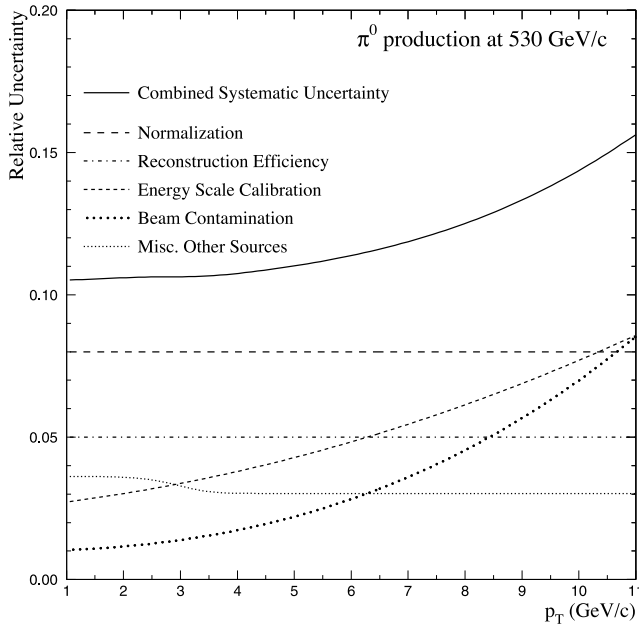


FIG. 13. Relative systematic uncertainty for π^0 production at 530 GeV/c as a function of p_T . Also shown are the contributions from the various sources of systematic uncertainty.

ing uncertainties at 800 GeV/c are comparable to those at 530 GeV/c. The uncertainties for η production are similar to those for π^0 production, except for the uncertainty in the trigger response, which is $\approx 5\%$ at low p_T . The actual systematic uncertainties are quoted in the appropriate tables of cross sections.

The secondary proton beam was determined to have a mean momentum of 530 ± 2 GeV/c with an estimated half-width of ≈ 30 GeV/c. This momentum spread introduces a small uncertainty ($\approx 5\%$) in comparisons of theory with data. For the 800 GeV primary beam, the momentum bite is very small and the corresponding uncertainty is negligible.

IV. INCLUSIVE CROSS SECTIONS

A. π^0 production

The inclusive π^0 cross sections per nucleon versus p_T , for protons on beryllium and liquid hydrogen targets, are shown in Figs. 14 and 15 for 530 and 800 GeV/c beams, respectively. Because of the steeply falling spectra, the data are plotted at abscissa values that correspond to the average values of the cross section in each p_T bin, assuming local exponential dependence on p_T [48]. These cross sections are also tabulated in Tables I and II. The corresponding cross sections as functions of p_T and y_{cm} are reported in Tables III–VI. For the values in the tables, the first uncertainty is statistical and the second is systematic; where only one uncertainty is presented, the statistical and systematic uncertainties have been combined because of the large correlation between them.

Ratios of inclusive π^0 cross sections per nucleon on Be target to those on p target are shown in Fig. 16. These ratios are compared with results from the HIJING Monte Carlo—a program designed to simulate particle production in pp , pA ,

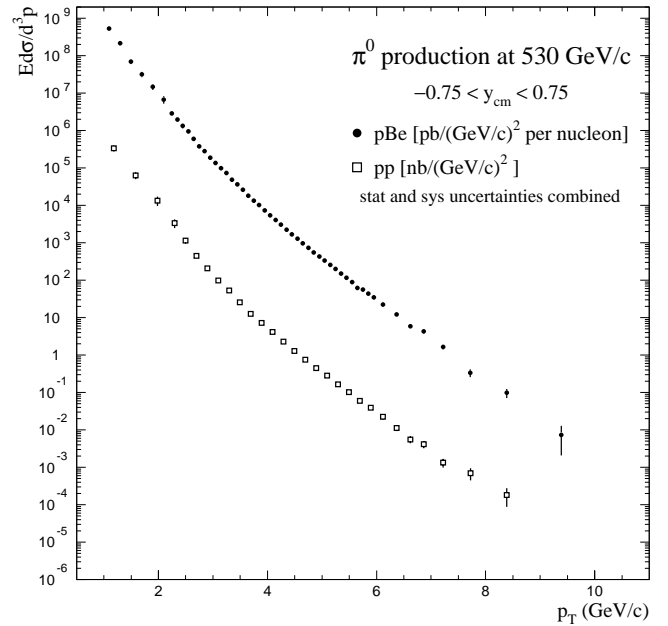


FIG. 14. Invariant differential cross sections (per nucleon) for π^0 production as a function of p_T in pp and pBe interactions at 530 GeV/c. Cross sections have been averaged over the full rapidity range, $-0.75 \leq y_{cm} \leq 0.75$. The error bars represent the combined statistical and systematic uncertainties.

and AA collisions [49,50]. The HIJING results are seen to be in good agreement with the data.

NLO PQCD calculations [3] are compared to data in Figs. 17–27. The PQCD calculations for the Be target have been

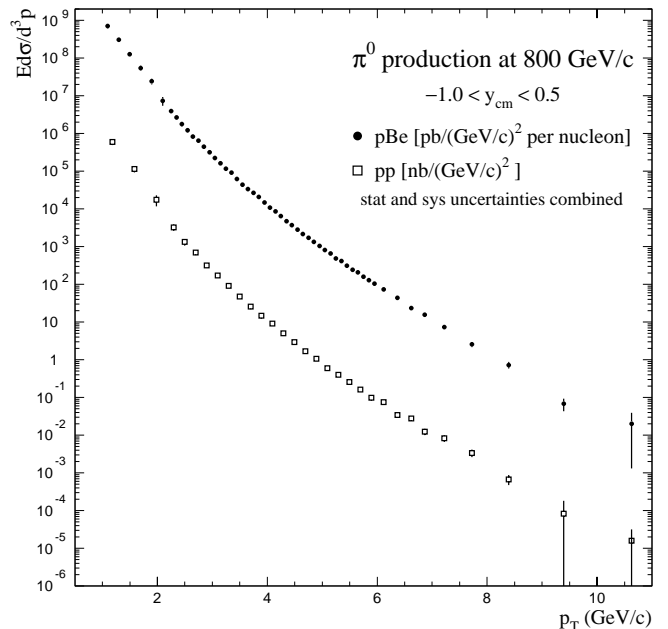


FIG. 15. Invariant differential cross sections (per nucleon) for π^0 production as a function of p_T in pp and pBe interactions at 800 GeV/c. Cross sections have been averaged over the full rapidity range, $-1.0 \leq y_{cm} \leq 0.5$. The error bars represent the combined statistical and systematic uncertainties.

TABLE I. Invariant inclusive differential cross sections ($E d\sigma/d^3p$) per nucleon for π^0 production in $p\text{Be}$ collisions at 530 and 800 GeV/ c , averaged over the rapidity intervals $-0.75 \leq y_{\text{cm}} \leq 0.75$ and $-1.0 \leq y_{\text{cm}} \leq 0.5$, respectively.

p_T (GeV/ c)	$p\text{Be}$ at 530 GeV/ c [$\mu\text{b}/(\text{GeV}/c)^2$]	$p\text{Be}$ at 800 GeV/ c [$\mu\text{b}/(\text{GeV}/c)^2$]
1.00–1.20	533±64	706±94
1.20–1.40	216±27	301±41
1.40–1.60	69±10	125±18
1.60–1.80	31.7±5.1	54.3±8.3
1.80–2.00	14.8±2.6	23.9±4.1
2.00–2.20	6.7±1.3±0.7	7.4±1.7±0.8
2.20–2.30	2.90±0.14±0.31	3.92±0.24±0.43
2.30–2.40	1.95±0.13±0.21	2.67±0.22±0.30
2.40–2.50	1.34±0.13±0.14	1.77±0.13±0.20
2.50–2.60	0.945±0.082±0.10	1.208±0.094±0.13
2.60–2.70	0.593±0.016±0.063	0.818±0.046±0.090
	[nb/(GeV/ c) ²]	[nb/(GeV/ c) ²]
2.70–2.80	374.3±9.7±40	649±33±72
2.80–2.90	280.9±8.9±30	448±10±49
2.90–3.00	189.6±6.8±20	317.0±7.3±35
3.00–3.10	136.1±3.1±14	221.8±5.3±24
3.10–3.20	97.3±2.7±10	161.7±4.5±18
3.20–3.30	73.1±2.3±7.8	116.2±3.3±13
3.30–3.40	47.9±1.4±5.1	91.6±3.2±10
3.40–3.50	35.9±1.5±3.8	62.1±2.2±6.8
3.50–3.60	25.91±0.98±2.8	43.9±1.8±4.8
3.60–3.70	17.99±0.81±1.9	33.6±1.6±3.7
3.70–3.80	13.32±0.50±1.4	26.4±1.2±2.9
3.80–3.90	10.19±0.29±1.1	20.6±1.0±2.3
3.90–4.00	7.367±0.055±0.79	14.56±0.76±1.6
4.00–4.10	5.415±0.041±0.58	10.86±0.44±1.2
4.10–4.20	4.054±0.032±0.44	8.59±0.12±0.95
4.20–4.30	3.064±0.026±0.33	6.443±0.096±0.71
4.30–4.40	2.236±0.021±0.24	4.706±0.073±0.52
4.40–4.50	1.686±0.017±0.18	3.657±0.067±0.41
4.50–4.60	1.281±0.014±0.14	2.831±0.054±0.32
4.60–4.70	0.970±0.012±0.11	2.159±0.046±0.24
	[pb/(GeV/ c) ²]	[pb/(GeV/ c) ²]
4.70–4.80	735±10±80	1727±37±190
4.80–4.90	557.1±8.3±61	1343±24±150
4.90–5.00	427.8±7.1±47	1049±22±120
5.00–5.10	335.9±6.3±37	811±18±91
5.10–5.20	254.1±5.2±28	658±17±74
5.20–5.30	198.0±4.8±22	486±16±55
5.30–5.40	150.6±3.9±17	411±13±46
5.40–5.50	117.0±3.4±13	312±10±35
5.50–5.60	88.9±2.9±10.0	243.7±7.8±28
5.60–5.70	62.4±2.5±7.0	207.1±6.8±24
5.70–5.80	55.8±2.3±6.3	159.5±6.1±18
5.80–5.90	43.5±2.0±4.9	128.6±5.6±15
5.90–6.00	35.1±1.8±4.0	103.4±5.3±12
6.00–6.25	22.44±0.85±2.6	74.3±2.0±8.5
6.25–6.50	12.06±0.61±1.4	43.9±1.6±5.1
6.50–6.75	5.88±0.41±0.69	23.5±1.1±2.7
6.75–7.00	4.31±0.35±0.51	15.58±0.83±1.8
7.00–7.50	1.66±0.15±0.20	7.31±0.40±0.87
7.50–8.00	0.335±0.065±0.041	2.56±0.25±0.31
8.00–9.00	0.098±0.023±0.013	0.72±0.11±0.09
9.00–10.00	0.0074±0.0053±0.0010	0.068±0.024±0.009
10.00–12.00		0.020±0.019±0.003

 TABLE II. Invariant inclusive differential cross sections ($E d\sigma/d^3p$) for π^0 production in pp collisions at 530 and 800 GeV/ c , averaged over the rapidity intervals $-0.75 \leq y_{\text{cm}} \leq 0.75$ and $-1.0 \leq y_{\text{cm}} \leq 0.5$, respectively.

p_T (GeV/ c)	pp at 530 GeV/ c [$\mu\text{b}/(\text{GeV}/c)^2$]	pp at 800 GeV/ c [$\mu\text{b}/(\text{GeV}/c)^2$]
1.00–1.40	335±58	590±100
1.40–1.80	63±12	114±21
1.80–2.20	13.4±3.8	17.3±5.5
2.20–2.40	3.35±0.80±0.36	3.25±0.43±0.36
2.40–2.60	1.15±0.14±0.12	1.33±0.22±0.15
	[nb/(GeV/ c) ²]	[nb/(GeV/ c) ²]
2.60–2.80	451±22±48	693±57±77
2.80–3.00	207±15±22	315±13±35
3.00–3.20	99.0±4.6±11	171.7±7.7±19
3.20–3.40	52.8±3.3±5.6	91.7±4.7±10
3.40–3.60	25.7±1.7±2.7	47.4±3.5±5.2
3.60–3.80	12.63±0.99±1.3	25.7±2.3±2.8
3.80–4.00	7.22±0.24±0.77	14.7±1.3±1.6
4.00–4.20	4.178±0.060±0.45	9.18±0.65±1.0
4.20–4.40	2.264±0.037±0.25	5.03±0.15±0.56
4.40–4.60	1.282±0.027±0.14	2.906±0.099±0.32
	[pb/(GeV/ c) ²]	[pb/(GeV/ c) ²]
4.60–4.80	758±18±83	1688±64±190
4.80–5.00	4451±13±50	1057±36±120
5.00–5.20	280.9±9.5±31	600±27±67
5.20–5.40	163.9±7.6±18	400±21±45
5.40–5.60	101.6±5.4±11	256±17±29
5.60–5.80	59.8±4.0±6.7	163±11±19
5.80–6.00	38.8±3.3±4.4	98.4±7.9±11
6.00–6.25	22.4±2.1±2.6	75.8±5.3±8.7
6.25–6.50	11.3±1.5±1.3	34.2±3.1±4.0
6.50–6.75	5.53±0.94±0.64	27.6±2.6±3.2
6.75–7.00	4.14±0.79±0.49	12.3±1.9±1.5
7.00–7.50	1.34±0.31±0.16	8.2±1.2±1.0
7.50–8.00	0.70±0.23±0.09	3.35±0.65±0.41
8.00–9.00	0.182±0.091±0.023	0.67±0.19±0.08
9.00–10.00		0.083±0.098±0.011
10.00–12.00		0.016±0.016±0.002

adjusted to account for nuclear effects using results from HIJING. In Fig. 17, NLO PQCD results using CTEQ4M parton distribution functions [51] and BKK fragmentation functions [52] are compared to the measured inclusive π^0 cross sections for $p\text{Be}$ and pp interactions at 800 GeV/ c . Theoretical results are presented for three values of factorization scale: $\mu = p_T/2$, p_T , and $2p_T$. In these comparisons, the renormalization and fragmentation scales have been set to the value of the factorization scale. In addition to a substantial dependence on choice of scale, the expectations for all these values of μ lie significantly below the data, for both 530 and 800 GeV/ c incident protons.

TABLE III. The averaged invariant differential cross section per nucleon ($Ed\sigma/d^3p$) as a function of rapidity and p_T for inclusive π^0 production in p Be collisions at 530 GeV/c.

y_{cm}	p_T (GeV/c)			
	1.00–1.50 [$\mu\text{b}/(\text{GeV}/c)^2$]	1.50–2.00 [$\mu\text{b}/(\text{GeV}/c)^2$]	2.00–2.50 [$\mu\text{b}/(\text{GeV}/c)^2$]	2.50–3.00 [nb/(GeV/c) ²]
–0.750––0.625	339±55	26.7±8.4	6.5±1.6±0.7	580±180±62
–0.625––0.500				409±86±44
–0.500––0.375	293±50	25.5±6.6	2.8±1.2±0.3	496±23±53
–0.375––0.250				494±15±53
–0.250––0.125	352±49	30.1±7.0	4.1±1.2±0.4	513±12±55
–0.125–0.000				587±13±62
0.000–0.125	278±42	33.0±6.6	5.1±1.2±0.5	528.1±9.8±56
0.125–0.250				502.1±8.2±53
0.250–0.375	297±43	31.5±5.9	2.7±1.3±0.3	454.9±7.6±48
0.375–0.500				427.5±7.5±45
0.500–0.625	346±46	16.6±5.3	2.27±0.97±0.24	387.1±8.0±41
0.625–0.750				341.3±7.8±36
	3.00–3.50 [nb/(GeV/c) ²]	3.50–4.00 [nb/(GeV/c) ²]	4.00–4.50 [nb/(GeV/c) ²]	4.50–5.00 [nb/(GeV/c) ²]
–0.750––0.625	69.3±4.6±7.4	9.61±0.66±1.0	2.531±0.065±0.27	0.586±0.020±0.064
–0.625––0.500	85.4±5.5±9.1	13.9±1.2±1.5	2.877±0.062±0.31	0.678±0.019±0.074
–0.500––0.375	79.1±5.1±8.4	14.4±1.0±1.5	3.264±0.053±0.35	0.783±0.018±0.086
–0.375––0.250	80.9±3.2±8.6	17.1±1.1±1.8	3.611±0.051±0.39	0.909±0.018±0.099
–0.250––0.125	89.9±3.3±9.6	17.8±1.1±1.9	3.873±0.042±0.42	0.964±0.017±0.11
–0.125–0.000	91.5±3.3±9.7	20.0±1.2±2.1	4.197±0.041±0.45	1.041±0.017±0.11
0.000–0.125	88.6±2.9±9.4	17.29±0.96±1.8	4.006±0.038±0.43	0.928±0.015±0.10
0.125–0.250	77.6±2.4±8.3	15.48±0.72±1.7	3.728±0.035±0.40	0.931±0.015±0.10
0.250–0.375	79.0±2.5±8.4	16.78±0.85±1.8	3.424±0.032±0.37	0.873±0.015±0.095
0.375–0.500	74.7±2.6±8.0	13.15±0.77±1.4	3.153±0.034±0.34	0.742±0.014±0.081
0.500–0.625	65.3±2.6±6.9	13.9±1.0±1.5	2.672±0.033±0.29	0.627±0.014±0.069
0.625–0.750	55.5±2.6±5.9	10.14±0.89±1.1	2.158±0.030±0.23	0.469±0.012±0.051
	5.00–5.50 [pb/(GeV/c) ²]	5.50–6.50 [pb/(GeV/c) ²]	6.50–8.00 [pb/(GeV/c) ²]	8.00–10.00 [pb/(GeV/c) ²]
–0.750––0.625	144.7±7.6±16	24.9±2.0±2.8	1.53±0.22±0.18	0.015±0.026±0.002
–0.625––0.500	202.9±8.6±22	28.9±1.9±3.3		
–0.500––0.375	216.5±7.7±24	40.1±2.1±4.6	2.04±0.23±0.24	0.053±0.026±0.007
–0.375––0.250	237.6±7.8±26	43.9±2.2±5.0		
–0.250––0.125	254.2±7.9±28	48.4±2.3±5.5	3.31±0.30±0.40	0.058±0.030±0.007
–0.125–0.000	269.0±8.2±30	50.4±2.3±5.7		
0.000–0.125	251.4±7.3±28	46.1±2.1±5.2	3.06±0.27±0.37	0.150±0.049±0.019
0.125–0.250	269.0±7.7±30	45.6±2.1±5.2		
0.250–0.375	230.5±7.2±26	42.8±2.0±4.9	2.68±0.28±0.32	0.029±0.021±0.004
0.375–0.500	183.2±6.6±20	34.7±1.9±3.9		
0.500–0.625	163.8±6.6±18	24.9±1.8±2.8	1.57±0.23±0.19	0.014±0.014±0.002
0.625–0.750	110.9±5.7±12	15.7±1.4±1.8		

In Fig. 18, NLO calculations using BKK and KKP [53] fragmentation functions, and $\mu = p_T/2$, are compared to the π^0 cross sections for 530 GeV/c p Be and pp interactions. Although the calculations exhibit considerable dependence on choice of fragmentation function, both choices predict yields that are significantly lower than the data.

These discrepancies have been interpreted [4–7] as arising from additional soft-gluon emission in the initial state that is not included in the NLO calculation, and which induces sizeable parton k_T prior to the hard collision (for a different perspective, see the discussion in Ref. [9]). Soft-gluon (or k_T) effects are expected in all hard-scattering pro-

TABLE IV. The averaged invariant differential cross section ($E d\sigma/d^3p$) as a function of rapidity and p_T for inclusive π^0 production in pp collisions at 530 GeV/c.

y_{cm}	p_T (GeV/c)			
	1.00–2.50 [$\mu\text{b}/(\text{GeV}/c)^2$]	2.50–3.00 [$\text{nb}/(\text{GeV}/c)^2$]	3.00–3.50 [$\text{nb}/(\text{GeV}/c)^2$]	3.50–4.00 [$\text{nb}/(\text{GeV}/c)^2$]
–0.750––0.625	176±43	430±200±46	68±10±7.2	8.7±1.4±0.9
–0.625––0.500		950±330±100	66±15±7.0	10.0±1.4±1.1
–0.500––0.375	118±36	367±40±39	62±10±6.6	12.3±2.7±1.3
–0.375––0.250		441±39±47	65.4±7.2±7.0	14.9±2.3±1.6
–0.250––0.125	76±32	458±26±49	76.6±6.9±8.1	15.4±2.4±1.7
–0.125–0.000		535±32±57	82.0±7.2±8.7	14.6±2.5±1.6
0.000–0.125	115±29	457±20±49	78.6±6.5±8.4	13.5±2.2±1.4
0.125–0.250		424±19±45	68.1±5.4±7.2	13.5±1.7±1.4
0.250–0.375	106±28	396±17±42	63.8±5.7±6.8	11.2±1.6±1.2
0.375–0.500		369±17±39	63.7±6.0±6.8	14.1±2.0±1.54
0.500–0.625	130±30	345±18±37	57.1±6.1±6.1	11.1±2.2±1.2
0.625–0.750		302±18±32	49.3±5.8±5.2	7.8±1.6±0.8
	4.00–4.50 [$\text{nb}/(\text{GeV}/c)^2$]	4.50–5.00 [$\text{nb}/(\text{GeV}/c)^2$]	5.00–5.50 [$\text{pb}/(\text{GeV}/c)^2$]	5.50–6.50 [$\text{pb}/(\text{GeV}/c)^2$]
–0.750––0.625	2.02±0.15±0.22	0.615±0.062±0.067	104±13±12	27.5±4.6±3.1
–0.625––0.500	2.46±0.14±0.27	0.515±0.046±0.056	166±21±18	21.0±4.2±2.4
–0.500––0.375	2.75±0.11±0.30	0.648±0.036±0.071	206±18±23	40.5±5.4±4.6
–0.375––0.250	3.34±0.12±0.36	0.836±0.046±0.091	193±17±21	40.1±5.0±4.6
–0.250––0.125	3.323±0.091±0.36	0.811±0.037±0.089	232±18±26	41.5±5.2±4.7
–0.125–0.000	3.568±0.095±0.39	0.919±0.040±0.10	239±19±26	62.8±6.4±7.1
0.000–0.125	3.570±0.092±0.39	0.809±0.034±0.088	267±19±30	52.0±5.5±5.9
0.125–0.250	3.315±0.083±0.36	0.848±0.037±0.093	251±18±28	52.4±5.6±5.9
0.250–0.375	2.975±0.073±0.32	0.724±0.033±0.079	235±18±26	38.6±4.8±4.4
0.375–0.500	2.794±0.078±0.30	0.683±0.033±0.075	199±17±22	31.2±4.3±3.5
0.500–0.625	2.360±0.075±0.25	0.623±0.034±0.068	178±17±20	25.3±4.2±2.9
0.625–0.750	1.921±0.069±0.21	0.449±0.030±0.049	117±14±13	21.7±4.1±2.5
	6.50–8.00 [$\text{pb}/(\text{GeV}/c)^2$]			
–0.750––0.625	2.00±0.57±0.24			
–0.625––0.500				
–0.500––0.375	2.61±0.66±0.31			
–0.375––0.250				
–0.250––0.125	2.99±0.70±0.36			
–0.125–0.000				
0.000–0.125	3.62±0.70±0.43			
0.125–0.250				
0.250–0.375	1.70±0.50±0.20			
0.375–0.500				
0.500–0.625	0.91±0.41±0.11			
0.625–0.750				

cesses, such as the inclusive production of jets, high- p_T mesons, and direct photons [54–57]. The Collins-Soper-Sterman resummation formalism [58] provides a rigorous basis for understanding these radiation effects, and there have been several recent efforts to derive resummation prescriptions for inclusive direct-photon [59–63], jet [64], and dijet

cross sections [65–67]. Compared to NLO calculations, the calculation of Ref. [59] for inclusive direct-photon production, which includes the effects of soft-gluon resummation near the kinematic threshold limit $x_T = 2p_T/\sqrt{s} \rightarrow 1$, has a far smaller sensitivity to scale, and provides cross sections close to those of NLO calculations with a scale of $\mu = p_T/2$. Also,

TABLE V. The averaged invariant differential cross sections per nucleon ($Ed\sigma/d^3p$) as a function of rapidity and p_T for inclusive π^0 production in $p\text{Be}$ collisions at 800 GeV/c.

y_{cm}	p_T (GeV/c)			
	1.00–1.50 [$\mu\text{b}/(\text{GeV}/c)^2$]	1.50–2.00 [$\mu\text{b}/(\text{GeV}/c)^2$]	2.00–2.50 [$\mu\text{b}/(\text{GeV}/c)^2$]	2.50–3.00 [$\text{nb}/(\text{GeV}/c)^2$]
–1.00––0.875	462±87	37±12	6.5±1.9±0.7	477±87±53
–0.875––0.750				840±180±92
–0.750––0.625	466±83	59±11	5.9±1.8±0.7	615±55±68
–0.625––0.500				686±50±76
–0.500––0.375	415±75	58±11	1.3±1.8±0.1	610±50±67
–0.375––0.250				705±51±78
–0.250––0.125	454±73	56±11	4.1±1.6±0.5	758±45±84
–0.125–0.000				732±46±81
0.000–0.125	423±66	45.8±9.3	5.4±1.6±0.6	766±47±85
0.125–0.250				730±100±81
0.250–0.375	491±70	31.9±8.5	4.5±1.4±0.5	750±49±83
0.375–0.500				588±42±65
	3.00–3.50 [$\text{nb}/(\text{GeV}/c)^2$]	3.50–4.00 [$\text{nb}/(\text{GeV}/c)^2$]	4.00–4.50 [$\text{nb}/(\text{GeV}/c)^2$]	4.50–5.00 [$\text{nb}/(\text{GeV}/c)^2$]
–1.00––0.875	100.5±8.1±11	20.0±2.0±2.2	4.01±0.28±0.44	1.039±0.036±0.12
–0.875––0.750	124.1±7.6±14	22.4±2.2±2.5	4.73±0.37±0.52	1.180±0.036±0.13
–0.750––0.625	102.3±6.1±11	25.8±2.5±2.8	5.58±0.31±0.62	1.512±0.038±0.17
–0.625––0.500	118.4±5.2±13	25.2±1.9±2.8	7.62±0.45±0.84	1.785±0.042±0.20
–0.500––0.375	143.0±6.4±16	30.0±2.1±3.3	7.40±0.40±0.82	2.029±0.037±0.23
–0.375––0.250	144.5±5.7±16	32.3±2.1±3.6	8.00±0.36±0.89	2.101±0.035±0.23
–0.250––0.125	149.0±5.7±16	28.1±2.2±3.1	7.91±0.32±0.88	2.168±0.036±0.24
–0.125–0.000	144.4±5.8±16	29.9±2.3±3.3	7.75±0.37±0.86	2.192±0.038±0.24
0.000–0.125	142.1±4.8±16	32.1±1.8±3.5	7.96±0.29±0.88	2.129±0.087±0.24
0.125–0.250	143.4±4.6±16	29.5±1.7±3.3	7.62±0.28±0.84	2.02±0.10±0.23
0.250–0.375	129.3±4.9±14	29.5±1.8±3.2	6.88±0.22±0.76	1.877±0.086±0.21
0.375–0.500	127.3±5.5±14	29.2±2.1±3.2	6.76±0.24±0.75	1.828±0.084±0.20
	5.00–5.50 [$\text{pb}/(\text{GeV}/c)^2$]	5.50–6.50 [$\text{pb}/(\text{GeV}/c)^2$]	6.50–8.00 [$\text{pb}/(\text{GeV}/c)^2$]	8.00–10.00 [$\text{pb}/(\text{GeV}/c)^2$]
–1.00––0.875	268±25±30	54.3±3.7±6.2	3.54±0.42±0.42	
–0.875––0.750	326±16±37	68.1±4.3±7.8		
–0.750––0.625	411±16±46	82.8±4.1±9.5	7.51±0.63±0.89	0.10±0.10±0.01
–0.625––0.500	505±19±57	109.3±5.6±13		
–0.500––0.375	595±18±67	120.5±4.9±14	11.18±0.70±1.3	0.50±0.11±0.06
–0.375––0.250	635±17±72	141.5±5.3±16		
–0.250––0.125	646±18±73	142.2±5.0±16	12.70±0.75±1.5	0.60±0.16±0.07
–0.125–0.000	639±19±72	135.2±5.2±15		
0.000–0.125	645±28±73	137.7±6.1±16	13.96±0.78±1.7	0.76±0.15±0.09
0.125–0.250	646±37±73	132.4±7.2±15		
0.250–0.375	583±29±66	134.1±6.5±15	9.93±0.73±1.2	0.48±0.16±0.06
0.375–0.500	526±27±59	107.0±6.0±12		

for our energies, the calculations of Ref. [68] using k_T -resummation, and of Refs. [62,63], which simultaneously treat threshold and recoil effects in direct-photon production, yield a substantially larger cross section than the NLO result. However, no such calculations are available for inclusive meson production. In their absence, we use a PQCD-based

model that incorporates transverse kinematics of initial-state partons to study the principal consequences of additional k_T for high- p_T production processes.

Because the unmodified PQCD cross sections fall rapidly with increasing p_T , the net effect of the “ k_T smearing” is to increase the expected yield at higher p_T . The modified par-

TABLE VI. The averaged invariant differential cross sections ($Ed\sigma/d^3p$) as a function of rapidity and p_T for inclusive π^0 production in pp collisions at 800 GeV/c.

y_{cm}	p_T (GeV/c)			
	1.00–2.50 [$\mu\text{b}/(\text{GeV}/c)^2$]	2.50–3.00 [$\text{nb}/(\text{GeV}/c)^2$]	3.00–3.50 [$\text{nb}/(\text{GeV}/c)^2$]	3.50–4.00 [$\text{nb}/(\text{GeV}/c)^2$]
–1.00––0.875	147±64	980±580±110	83±16±9.1	19.2±7.4±2.1
–0.875––0.750		410±110±45	108±14±12	18.7±4.1±2.1
–0.750––0.625	225±64	420±63±46	101±14±11	36.9±6.9±4.1
–0.625––0.500		570±100±63	111±12±12	18.0±3.6±2.0
–0.500––0.375	269±62	560±110±62	144±14±16	26.6±5.5±2.9
–0.375––0.250		600±99±66	130±13±14	37.1±6.0±4.1
–0.250––0.125	254±57	760±170±84	117±14±13	31.0±5.2±3.4
–0.125–0.000		640±110±71	117±12±13	20.6±4.1±2.3
0.000–0.125	190±47	669±95±74	127±11±14	23.7±4.5±2.6
0.125–0.250		720±110±80	130±10±14	26.3±4.0±2.9
0.250–0.375	222±47	511±84±57	115±11±13	22.5±3.6±2.5
0.375–0.500		699±97±77	102±12±11	22.4±5.1±2.5
	4.00–4.50 [$\text{nb}/(\text{GeV}/c)^2$]	4.50–5.00 [$\text{nb}/(\text{GeV}/c)^2$]	5.00–5.50 [$\text{pb}/(\text{GeV}/c)^2$]	5.50–6.50 [$\text{pb}/(\text{GeV}/c)^2$]
–1.00––0.875	3.02±0.25±0.34	1.18±0.12±0.13	280±46±32	30.3±5.2±3.5
–0.875––0.750	4.66±0.65±0.52	0.957±0.072±0.11	217±25±24	70±13±8.0
–0.750––0.625	8.4±2.2±0.9	1.350±0.085±0.15	331±34±37	60.2±8.2±6.9
–0.625––0.500	7.4±1.5±0.8	1.504±0.093±0.17	423±36±48	99±12±11
–0.500––0.375	6.41±0.63±0.71	1.808±0.087±0.20	479±41±54	84.9±9.7±9.7
–0.375––0.250	6.86±0.61±0.76	1.901±0.081±0.21	517±39±58	124±12±14
–0.250––0.125	6.00±0.20±0.66	1.963±0.083±0.22	595±41±67	110±11±13
–0.125–0.000	6.14±0.35±0.68	1.878±0.081±0.21	552±38±62	140±13±16
0.000–0.125	8.2±1.0±0.9	1.49±0.13±0.17	607±68±68	150±17±17
0.125–0.250	6.19±0.57±0.69	1.71±0.22±0.19	567±88±64	111±14±13
0.250–0.375	47.08±0.57±0.78	1.68±0.20±0.19	459±61±52	97±12±11
0.375–0.500	5.69±0.52±0.63	1.81±0.21±0.20	502±64±57	129±16±15
	6.50–8.00 [$\text{pb}/(\text{GeV}/c)^2$]	8.00–10.00 [$\text{pb}/(\text{GeV}/c)^2$]		
–1.00––0.875	4.20±1.00±0.50	0.085±0.085±0.010		
–0.875––0.750				
–0.750––0.625	8.8±1.6±1.0	0.23±0.17±0.03		
–0.625––0.500				
–0.500––0.375	14.0±1.8±1.7	0.53±0.24±0.07		
–0.375––0.250				
–0.250––0.125	13.8±1.7±1.6	0.95±0.43±0.12		
–0.125–0.000				
0.000–0.125	12.7±2.1±1.5	0.66±0.30±0.08		
0.125–0.250				
0.250–0.375	9.6±1.7±1.1			
0.375–0.500				

ton kinematics have been implemented in a Monte Carlo calculation of the leading-order (LO) cross sections for high- p_T particle production [69], with the k_T distribution for each of the incoming partons represented by a Gaussian with $\langle k_T \rangle$ as an adjustable parameter. Unfortunately, no such program is available for NLO calculations, and so we approxi-

mate the effect of k_T smearing by multiplying the NLO cross sections by the corresponding LO k_T -enhancement factors. Admittedly, this procedure involves a risk of double-counting since some of the k_T -enhancement may already be contained in the NLO calculation. However, we expect the effects of such double-counting to be small.

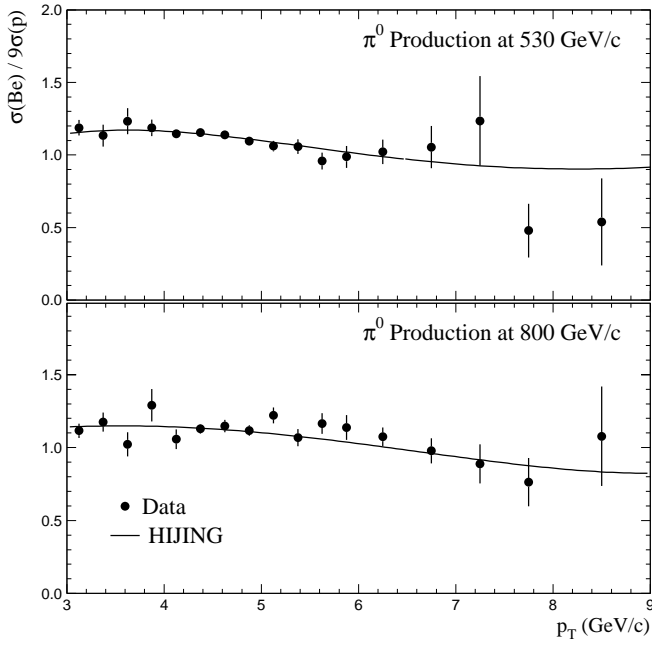


FIG. 16. The ratio of inclusive π^0 production cross sections per nucleon in $p\text{Be}$ to those in pp collisions, compared with predictions from HIJING. The error bars represent only statistical contributions to the uncertainties.

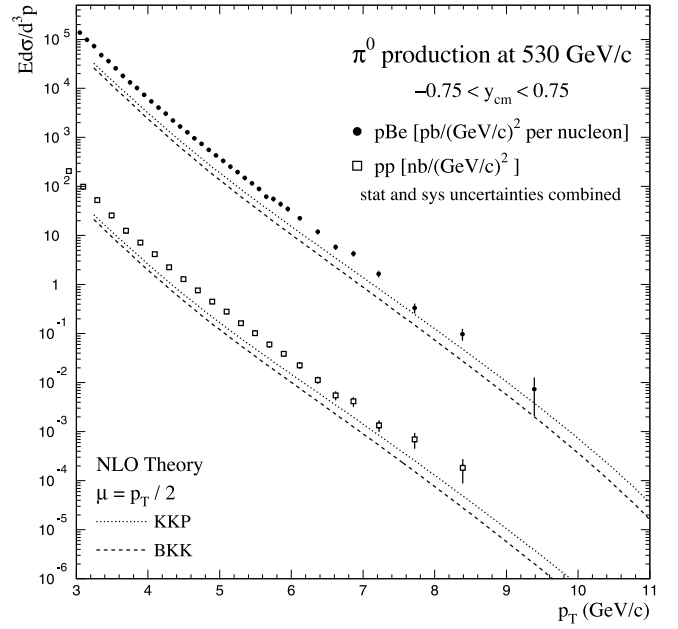


FIG. 18. Invariant differential cross sections (per nucleon) for π^0 production as a function of p_T in $p\text{Be}$ and pp interactions at 530 GeV/c, compared to NLO PQCD calculations, with scale $\mu = p_T/2$, for BKK as well as KKP fragmentation functions. The NLO calculations on Be have been adjusted for nuclear effects. The error bars have statistical and systematic uncertainties added in quadrature.

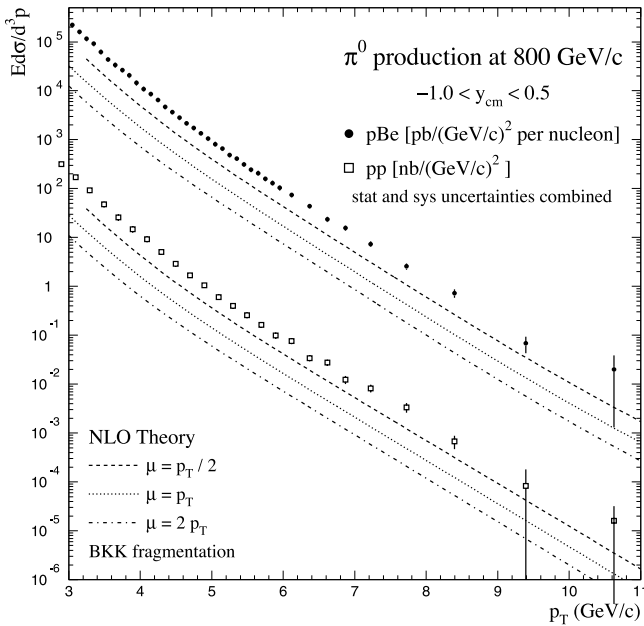


FIG. 17. Invariant differential cross sections (per nucleon) for π^0 production as a function of p_T in $p\text{Be}$ and pp interactions at 800 GeV/c, compared to NLO PQCD calculations, with scale choices of $\mu = p_T/2$, p_T , and $2p_T$. The NLO calculations on Be have been adjusted for nuclear effects. The error bars have statistical and systematic uncertainties added in quadrature.

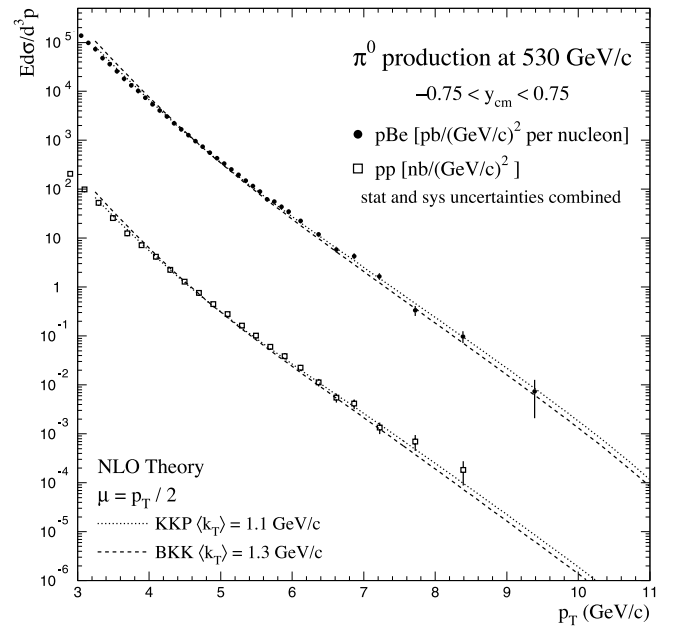


FIG. 19. Invariant differential cross sections (per nucleon) for π^0 production as a function of p_T in $p\text{Be}$ and pp interactions at 530 GeV/c, compared to k_T -enhanced NLO PQCD calculations with scale $\mu = p_T/2$. Comparisons are shown for both BKK and KKP fragmentation functions. The NLO calculations on Be have been adjusted for nuclear effects. The error bars have statistical and systematic uncertainties added in quadrature.

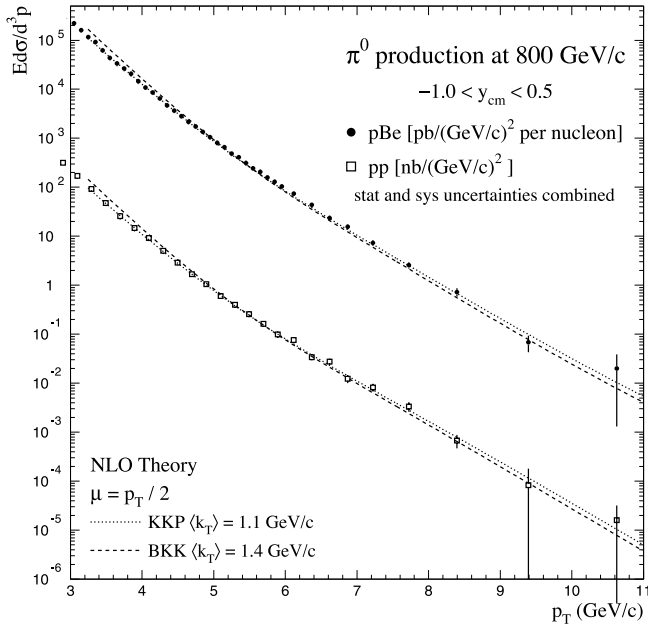


FIG. 20. Invariant differential cross sections (per nucleon) for π^0 production as a function of p_T in $p\text{Be}$ and pp interactions at 800 GeV/c, compared to k_T -enhanced NLO PQCD calculations, with scale $\mu = p_T/2$. Comparisons are shown for both BKK and KKP fragmentation functions. The NLO calculations on Be have been adjusted for nuclear effects. The error bars have statistical and systematic uncertainties added in quadrature.

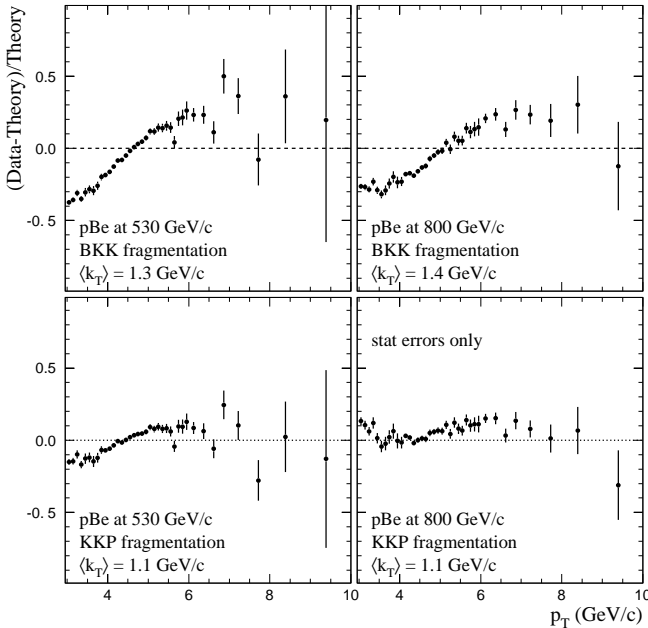


FIG. 21. Fractional difference between data and k_T -enhanced NLO PQCD calculations for π^0 production in $p\text{Be}$ interactions at 530 and 800 GeV/c as a function of p_T . The NLO calculations on Be have been adjusted for nuclear effects. The error bars represent only statistical contributions to the uncertainties.

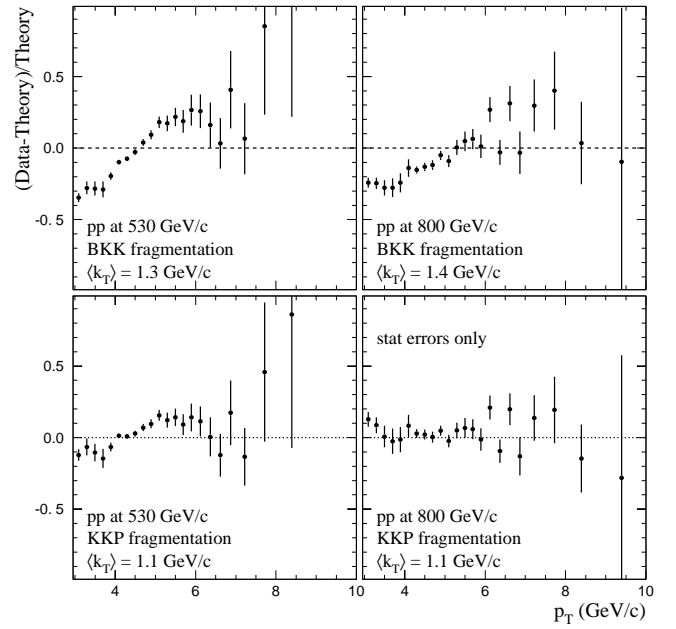


FIG. 22. Fractional difference between data and k_T -enhanced NLO PQCD results for π^0 production in pp interactions at 530 and 800 GeV/c as a function of p_T . The error bars represent only statistical contributions to the uncertainties.

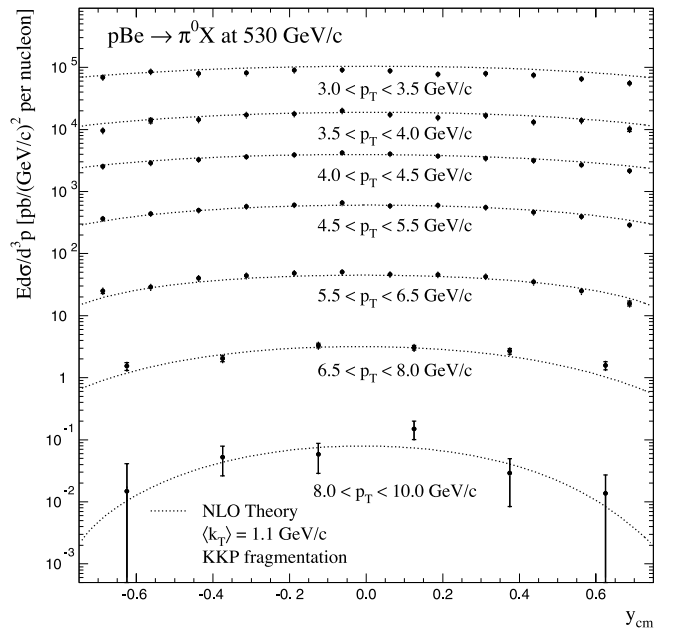


FIG. 23. Invariant cross sections per nucleon for π^0 production in $p\text{Be}$ interactions at 530 GeV/c. Cross sections are shown versus y_{cm} for several intervals in p_T . The curves represent the k_T -enhanced NLO QCD calculations for $\langle k_T \rangle = 1.1$ GeV/c and $\mu = p_T/2$, using KKP fragmentation functions, and have been adjusted for nuclear effects. The error bars have statistical and systematic uncertainties added in quadrature.

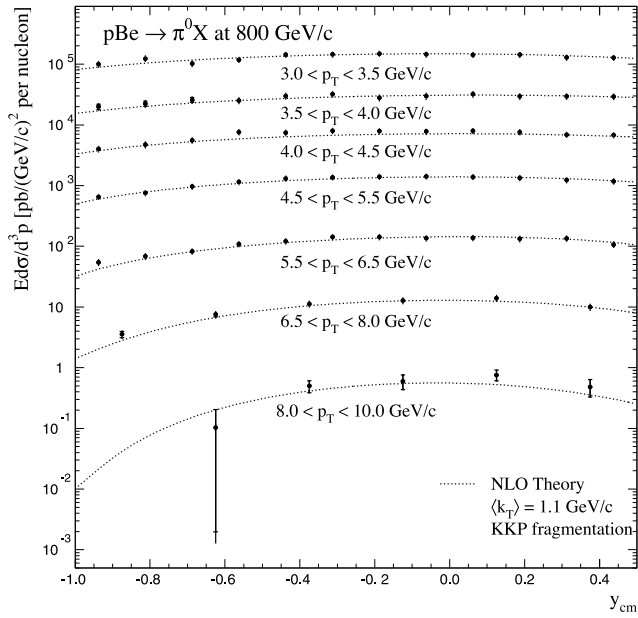


FIG. 24. Invariant cross section per nucleon for π^0 production in $p\text{Be}$ interactions at 800 GeV/c. Cross sections are shown versus y_{cm} for several intervals in p_T . The curves represent the k_T -enhanced NLO QCD calculations for $\langle k_T \rangle = 1.1$ GeV/c and $\mu = p_T/2$, using KKP fragmentation functions, and have been adjusted for nuclear effects. The error bars have statistical and systematic uncertainties added in quadrature.

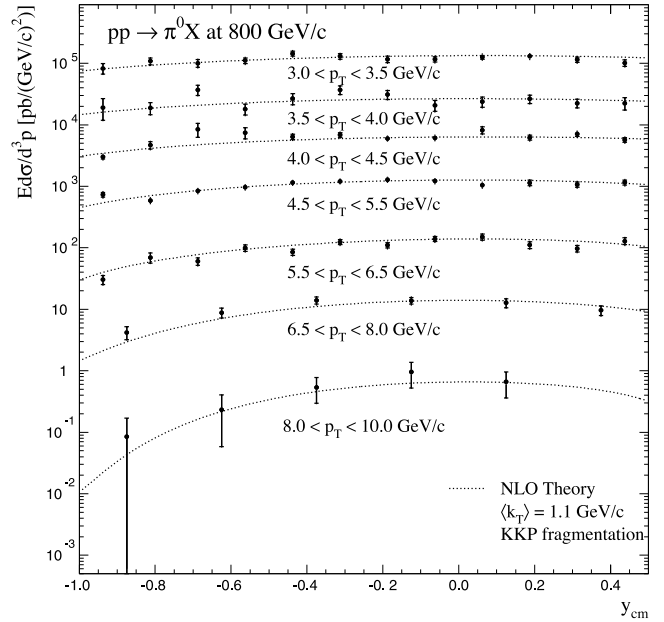


FIG. 26. Invariant cross section for π^0 production in pp interactions at 800 GeV/c. Cross sections are shown versus y_{cm} for several intervals in p_T . The curves represent the k_T -enhanced NLO QCD calculations for $\langle k_T \rangle = 1.1$ GeV/c and $\mu = p_T/2$, using KKP fragmentation functions. The error bars have statistical and systematic uncertainties added in quadrature.

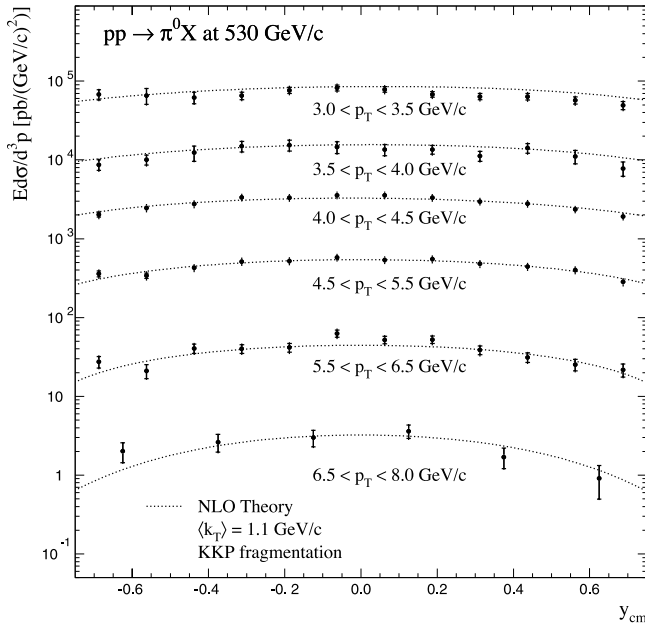


FIG. 25. Invariant cross sections for π^0 production in pp interactions at 530 GeV/c. Cross sections are shown versus y_{cm} for several intervals in p_T . The curves represent the k_T -enhanced NLO QCD calculations for $\langle k_T \rangle = 1.1$ GeV/c and $\mu = p_T/2$, using KKP fragmentation functions. The error bars have statistical and systematic uncertainties added in quadrature.

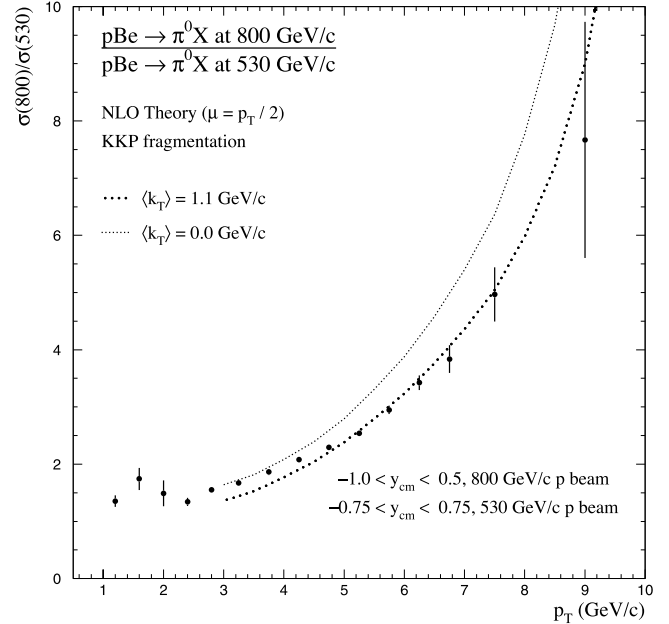


FIG. 27. Ratio of invariant cross sections for π^0 production in $p\text{Be}$ interactions at 800 and 530 GeV/c as a function of p_T , compared to conventional and k_T -enhanced NLO QCD calculations using KKP fragmentation functions. The NLO calculations have been adjusted for nuclear effects. The error bars reflect only statistical uncertainties for $p_T > 2$ GeV/c.

The $\langle k_T \rangle$ values used in the calculation of the LO k_T -enhancement factors are similar to those employed in comparisons of kinematic distributions in data involving production of high-mass $\gamma\gamma$, $\gamma\pi^0$, and $\pi^0\pi^0$ systems, and rely on the same LO program (see Refs. [4–6] for further details). For these comparisons, we used the LO versions of the CTEQ4 distribution, BKK fragmentation functions, and an average transverse momentum of 0.6 GeV/ c for π^0 mesons relative to the fragmenting parton direction (varying this parameter in the range 0.3 to 0.7 GeV/ c does not affect our conclusions) [70,71].

Comparisons of the k_T -enhanced calculations with data at 530 GeV/ c are displayed in Fig. 19, indicating reasonable agreement for the chosen $\langle k_T \rangle$ values. Similar conclusions can be drawn from comparisons between calculations and data at 800 GeV/ c , as illustrated in Fig. 20. A comparison on a linear scale of the fractional differences between data and the k_T -enhanced NLO calculations using BKK and KKP fragmentation functions is shown in Fig. 21 for p Be interactions at 530 and 800 GeV/ c . The k_T -enhanced calculations using the KKP fragmentation functions are seen to reproduce the shape of the π^0 cross section better than calculations using the earlier BKK fragmentation functions. Similar conclusions can be drawn from comparisons of NLO QCD with our data on pp collisions (Fig. 22).

Figures 23 through 26 show the cross sections for inclusive π^0 production as functions of rapidity for p Be and pp interactions at 530 and 800 GeV/ c , for several intervals in p_T . The peaking expected at a scattering angle near 90° in the center of mass ($y_{\text{cm}}=0$) develops slowly as a function of p_T . The shapes and normalizations of the data are in good agreement with the k_T -enhanced calculations.

Both theoretical and experimental uncertainties are reduced in the ratio of invariant cross sections for π^0 production at 800 and 530 GeV/ c , allowing, in principle, a more sensitive test of the calculations. Figure 27 displays this ratio compared to the conventional $\langle k_T \rangle=0$ and k_T -enhanced NLO results using KKP fragmentation functions. The $\langle k_T \rangle$ values are those used in Figs. 19 and 20. The energy dependence of the data is accommodated better by the k_T -enhanced theory. Similar results are obtained for the data on the hydrogen target (not shown).

The results discussed in this section are not very sensitive to the specific parton distribution functions used in the calculations [4], the quark distributions being of primary importance here. Methods similar to the ones described in this paper have been applied to analyze high- p_T hadron spectra in pp , pA , and AA collisions, and k_T effects have been found important for describing data on inclusive production of charged mesons [49,72].

B. η production

Cross sections for inclusive η production are tabulated in Tables VII–XII. Theoretical descriptions of η -meson production differ from the π^0 case primarily because of differences in the fragmentation of partons into the particles of interest. To investigate this aspect, we present η/π^0 relative

TABLE VII. Invariant inclusive differential cross sections ($E d\sigma/d^3p$) per nucleon for η production in p Be collisions at 530 and 800 GeV/ c , averaged over the rapidity intervals $-0.75 \leq y_{\text{cm}} \leq 0.75$ and $-1.0 \leq y_{\text{cm}} \leq 0.5$, respectively.

p_T (GeV/ c)	p Be at 530 GeV/ c [nb/(GeV/ c) 2]	p Be at 800 GeV/ c [nb/(GeV/ c) 2]
3.00–3.20	$49.8 \pm 9.0 \pm 6.0$	$88 \pm 18 \pm 11$
3.20–3.40	$24.3 \pm 4.5 \pm 2.9$	$34.7 \pm 8.5 \pm 4.3$
3.40–3.60	$16.7 \pm 2.5 \pm 2.0$	$19.5 \pm 5.1 \pm 2.4$
3.60–3.80	$8.5 \pm 1.4 \pm 1.0$	$8.1 \pm 3.0 \pm 1.0$
3.80–4.00	$3.68 \pm 0.25 \pm 0.42$	$7.34 \pm 0.77 \pm 0.86$
4.00–4.20	$2.00 \pm 0.13 \pm 0.23$	$3.89 \pm 0.33 \pm 0.45$
4.20–4.40	$1.247 \pm 0.078 \pm 0.14$	$2.18 \pm 0.19 \pm 0.25$
4.40–4.60	$0.586 \pm 0.043 \pm 0.067$	$1.20 \pm 0.12 \pm 0.14$
4.60–4.80	$0.411 \pm 0.024 \pm 0.047$	$0.805 \pm 0.073 \pm 0.095$
4.80–5.00	$0.244 \pm 0.017 \pm 0.028$	$0.502 \pm 0.048 \pm 0.059$
	[pb/(GeV/ c) 2]	[pb/(GeV/ c) 2]
5.00–5.25	$132.6 \pm 9.2 \pm 15$	$341 \pm 27 \pm 40$
5.25–5.50	$70.0 \pm 5.6 \pm 8.2$	$152 \pm 15 \pm 18$
5.50–5.75	$36.5 \pm 4.4 \pm 4.3$	$107 \pm 12 \pm 13$
5.75–6.00	$16.5 \pm 2.3 \pm 2.0$	$58.0 \pm 8.0 \pm 7.0$
6.00–6.50	$7.25 \pm 0.97 \pm 0.87$	$26.3 \pm 3.6 \pm 3.2$
6.50–7.00	$2.63 \pm 0.43 \pm 0.32$	$10.4 \pm 1.8 \pm 1.3$
7.00–8.00	$0.22 \pm 0.13 \pm 0.03$	$3.02 \pm 0.64 \pm 0.38$
8.00–9.00	$0.034 \pm 0.046 \pm 0.005$	$1.33 \pm 0.43 \pm 0.17$
9.00–10.00		$0.11 \pm 0.24 \pm 0.02$
10.00–12.00		$0.073 \pm 0.050 \pm 0.010$

production rates as functions of p_T and y_{cm} (for two ranges of p_T) in Figs. 28 and 29—the average value of the ratio for $3 < p_T < 8$ GeV/ c is 0.45 ± 0.01 at 530 GeV/ c , and 0.42 ± 0.01 at 800 GeV/ c .

TABLE VIII. Invariant inclusive differential cross sections ($E d\sigma/d^3p$) for η production in pp collisions at 530 and 800 GeV/ c , averaged over the rapidity intervals $-0.75 \leq y_{\text{cm}} \leq 0.75$ and $-1.0 \leq y_{\text{cm}} \leq 0.5$, respectively.

p_T (GeV/ c)	pp at 530 GeV/ c [nb/(GeV/ c) 2]	pp at 800 GeV/ c [nb/(GeV/ c) 2]
3.00–3.50	$22.5 \pm 9.5 \pm 2.7$	$51 \pm 17 \pm 6.3$
3.50–4.00	$7.6 \pm 1.9 \pm 0.9$	$11.4 \pm 3.7 \pm 1.4$
4.00–4.50	$1.19 \pm 0.14 \pm 0.14$	$2.13 \pm 0.34 \pm 0.25$
4.50–5.00	$0.311 \pm 0.035 \pm 0.036$	$0.678 \pm 0.091 \pm 0.080$
	[pb/(GeV/ c) 2]	[pb/(GeV/ c) 2]
5.00–5.50	$78 \pm 12 \pm 9.1$	$220 \pm 36 \pm 26$
5.50–6.00	$24.1 \pm 5.0 \pm 2.9$	$108 \pm 16 \pm 13$
6.00–7.00	$2.4 \pm 1.3 \pm 0.3$	$20.6 \pm 4.8 \pm 2.5$
7.00–8.00	$0.41 \pm 0.31 \pm 0.05$	$4.4 \pm 1.8 \pm 0.6$
8.00–10.00		$1.05 \pm 0.70 \pm 0.14$

TABLE IX. The averaged invariant differential cross sections per nucleon ($Ed\sigma/d^3p$) as a function of rapidity and p_T for inclusive η production in $p\text{Be}$ collisions at 530 GeV/c. The units are pb/(GeV/c)².

y_{cm}	p_T (GeV/c)		
	3.00–4.00	4.00–4.50	4.50–5.00
–0.750––0.625	14900±9000±1800	1050±310±120	246±62±28
–0.625––0.500		960±320±110	318±88±37
–0.500––0.375	24700±5000±2900	1420±280±160	376±68±43
–0.375––0.250		1740±290±200	424±60±49
–0.250––0.125	21400±3800±2500	1910±250±220	485±57±56
–0.125–0.000		1740±200±200	516±56±59
0.000–0.125	26400±3400±3100	1330±170±150	484±51±56
0.125–0.250		2060±160±240	365±45±42
0.250–0.375	22700±3300±2700	1480±120±170	332±39±38
0.375–0.500		1400±100±160	341±36±39
0.500–0.625	13400±4100±1600	1230±100±140	322±36±37
0.625–0.750		833±74±95	187±28±22
	5.00–5.50	5.50–6.50	6.50–8.00
–0.750––0.625	65±25±7.5	4.6±7.0±0.6	0.35±0.33±0.04
–0.625––0.500	95±20±11	13.6±3.9±1.6	
–0.500––0.375	100±26±12	7.6±6.9±0.9	1.03±0.46±0.13
–0.375––0.250	109±18±13	16.3±4.3±1.9	
–0.250––0.125	135±19±16	21.1±4.6±2.5	1.59±0.46±0.20
–0.125–0.000	124±17±14	19.5±4.4±2.3	
0.000–0.125	121±18±14	21.6±4.2±2.6	1.68±0.45±0.21
0.125–0.250	98±15±11	20.2±4.0±2.4	
0.250–0.375	128±20±15	23.8±3.8±2.8	0.82±0.41±0.10
0.375–0.500	94±15±11	19.9±3.8±2.4	
0.500–0.625	91±14±11	18.5±3.3±2.2	0.68±0.33±0.08
0.625–0.750	56±12±6.5	14.4±3.2±1.7	

TABLE X. The averaged invariant differential cross sections ($Ed\sigma/d^3p$) as a function of rapidity and p_T for inclusive η production in pp collisions at 530 GeV/c. The units are pb/(GeV/c)².

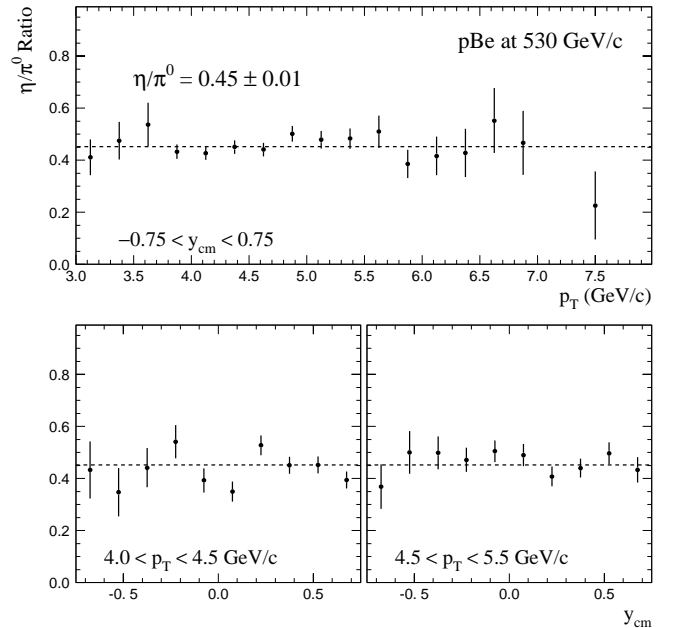
y_{cm}	p_T (GeV/c)		
	4.00–5.00	5.00–6.00	6.00–8.00
–0.75––0.50	540±250±62	29±19±3.4	1.6±1.0±0.2
–0.50––0.25	700±230±80	53±16±6.2	
–0.25–0.00	1160±190±130	58±16±6.8	1.3±1.1±0.2
0.00–0.25	740±150±84	70±18±8.2	
0.25–0.50	800±110±92	46±13±5.4	1.3±1.2±0.2
0.50–0.75	568±73±65	49±13±5.8	

TABLE XI. The averaged invariant differential cross sections per nucleon ($Ed\sigma/d^3p$) as a function of rapidity and p_T for inclusive η production in $p\text{Be}$ collisions at 800 GeV/c. The units are $\text{pb}/(\text{GeV}/c)^2$.

y_{cm}	p_T (GeV/c)			
	3.00–4.00	4.00–4.50	4.50–5.00	5.00–5.50
–1.00––0.875	13000±15000±1600	920±580±110		116±47±14
–0.875––0.750		1360±620±160	500±240±58	87±52±10
–0.750––0.625	46000±11000±5600	1980±630±230	560±130±65	155±43±18
–0.625––0.500		1270±580±150	540±160±64	259±48±31
–0.500––0.375	17300±8100±2100	2330±550±270	640±120±76	299±49±35
–0.375––0.250		3840±530±450	710±150±84	253±56±30
–0.250––0.125	48200±8800±5800	3520±570±410	570±130±67	239±48±28
–0.125–0.000		4130±520±480	940±140±110	292±53±35
0.000–0.125	34500±6700±4200	4070±600±480	1200±160±140	311±64±37
0.125–0.250		2840±510±330	1220±180±140	386±76±46
0.250–0.375	29000±7100±3500	3670±350±430	1170±130±140	275±57±33
0.375–0.500		2230±260±260	1090±110±130	282±48±33
	5.50–6.50	6.50–8.00	8.00–10.00	
–1.00––0.875	9±10±1.1		1.50±0.93±0.20	
–0.875––0.750	22.5±8.9±2.7			
–0.750––0.625	51±16±6.1	6.8±2.0±0.8	0.52±0.93±0.07	
–0.625––0.500	41±11±4.9			
–0.500––0.375	34±12±4.1	4.3±1.6±0.5	0.55±0.52±0.07	
–0.375––0.250	51±11±6.1			
–0.250––0.125	86±16±10	6.4±1.5±0.8	0.68±0.23±0.09	
–0.125–0.000	79±13±9.5			
0.000–0.125	93±17±11	8.3±2.2±1.0	0.61±0.28±0.08	
0.125–0.250	70±18±8.4			
0.250–0.375	61±15±7.3	7.4±1.8±0.9	0.48±0.27±0.06	
0.375–0.500	54±13±6.5			

 TABLE XII. The averaged invariant differential cross sections ($Ed\sigma/d^3p$) as a function of rapidity and p_T for inclusive η production in pp collisions at 800 GeV/c. The units are $\text{pb}/(\text{GeV}/c)^2$.

y_{cm}	p_T (GeV/c)		
	4.00–5.00	5.00–6.00	6.00–8.00
–1.0––0.75	1060±430±120	73±50±8.7	6.9±3.6±0.8
–0.75––0.50	360±520±42	97±49±12	4.9±7.1±0.6
–0.50––0.25	1930±420±230	194±40±23	14.4±7.6±1.8
–0.25–0.00	1880±440±220	256±47±31	22.3±6.0±2.7
0.00–0.25	1980±470±230	167±55±20	16.9±7.6±2.1
0.25–0.50	1230±250±140	198±50±24	9.6±5.0±1.2


 FIG. 28. Ratios of η to π^0 invariant cross sections for 530 GeV/c $p\text{Be}$ interactions, as a function of p_T (top), and of y_{cm} (bottom) for two p_T ranges. The error bars reflect only statistical uncertainties.

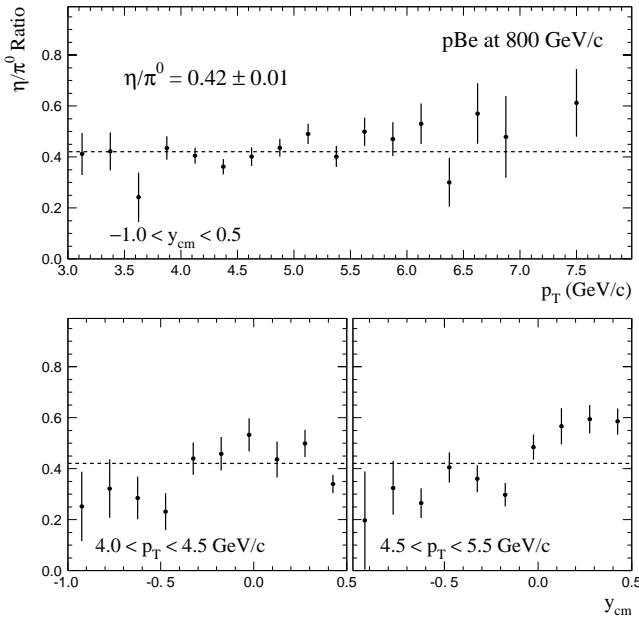


FIG. 29. Ratios of η to π^0 invariant cross sections for 800 GeV/c $p\text{Be}$ interactions, as a function of p_T (top), and of y_{cm} (bottom) for two p_T ranges. The error bars reflect only statistical uncertainties.

V. SUMMARY

The invariant cross sections for π^0 and η production have been measured in pp and $p\text{Be}$ collisions at 530 and 800 GeV/c as functions of p_T and y_{cm} , over the kinematic range $1 < p_T < 10$ GeV/c, and 1.5 units in rapidity. Results from k_T -enhanced NLO QCD calculations are in reasonable agreement with our measured π^0 cross sections. Employing the recent KKP fragmentation functions in the NLO QCD calculations was found to improve the description of the detailed shape of our π^0 cross sections as a function of

p_T relative to theoretical results obtained using the earlier BKK fragmentation functions. The η/π^0 production ratio, which provides information about the relative fragmentation of partons into these mesons, was measured at 530 and 800 GeV/c.

ACKNOWLEDGMENTS

We thank the U. S. Department of Energy, the National Science Foundation, including its Office of International Programs and the Universities Grants Commission of India, for their support of this research. The staff and management of Fermilab are thanked for their efforts in making available the beam and computing facilities that made this work possible. We are also pleased to acknowledge contributions of our colleagues on Fermilab experiment E672, and the following colleagues who contributed during the upgrade and operation of the Meson West spectrometer: W. Dickerson, E. Pothier from Northeastern University; J. T. Anderson, E. Barsotti, Jr., H. Koecher, P. Madsen, D. Petravick, R. Tokarek, J. Tweed, D. Allspach, J. Urbin, R. L. Schmitt and the cryo crews from Fermi National Accelerator Laboratory. We thank T. Haelen, C. Benson, L. Kuntz, and D. Ruggiero from the University of Rochester, and the technical staffs of Michigan State University and Pennsylvania State University for their help and dedication in the construction of the detectors for this experiment. We would also like to thank the following commissioning run collaborators for their invaluable contributions to the hardware and software infrastructure of the original Meson West spectrometer: G. Alverson, G. Balocchi, R. Benson, D. Berg, D. Brown, D. Carey, T. Chand, C. Chandlee, S. Easo, W. Faissler, G. Glass, I. Kourbanis, A. Lanaro, C. A. Nelson, Jr., D. Orris, B. M. Rajaram, K. Ruddick, A. Sinanidis, and G. Wu. Finally, we thank S. Catani, J.Ph. Guillet, B. Kniehl, J. Owens, G. Sterman, W. Vogelsang, and X.-N. Wang for many helpful discussions and for providing us with their QCD calculations.

[1] W.M. Geist *et al.*, Phys. Rep. **197**, 263 (1990).
 [2] N.A. McCubbin, Rep. Prog. Phys. **44**, 65 (1981).
 [3] F. Aversa *et al.*, Nucl. Phys. **B327**, 105 (1989).
 [4] L. Apanasevich *et al.*, Phys. Rev. Lett. **81**, 2642 (1998).
 [5] L. Apanasevich *et al.*, Phys. Rev. D **59**, 074007 (1999).
 [6] L. Apanasevich *et al.*, Phys. Rev. D **63**, 014009 (2001).
 [7] J. Huston *et al.*, Phys. Rev. D **51**, 6139 (1995).
 [8] P. Aurenche *et al.*, Eur. Phys. J. C **9**, 107 (1999).
 [9] P. Aurenche *et al.*, Eur. Phys. J. C **13**, 347 (2000).
 [10] k_T denotes the magnitude of the effective transverse momentum vector, \vec{k}_T , of each of the two colliding partons.
 [11] J. Breitweg *et al.*, Phys. Lett. B **472**, 175 (2000).
 [12] J. Breitweg *et al.*, Phys. Lett. B **511**, 19 (2001).
 [13] M. Fontannaz, J.P. Guillet, and G. Heinrich, Eur. Phys. J. C **21**, 303 (2001).
 [14] M. Fontannaz, J.P. Guillet, and G. Heinrich, Eur. Phys. J. C **22**, 303 (2001).
 [15] A. Zembruski and M. Krawczyk, Phys. Rev. D **64**, 114017 (2001).
 [16] J.F. Owens, Phys. Rev. D **65**, 034011 (2002).
 [17] G. Alverson *et al.*, Phys. Rev. D **48**, 5 (1993).
 [18] G. Alverson *et al.*, Phys. Rev. D **45**, 3899 (1992).
 [19] G. Alverson *et al.*, Phys. Rev. Lett. **68**, 2584 (1992).
 [20] G. Alverson *et al.*, Phys. Rev. D **49**, 3106 (1994).
 [21] D. Striley, Ph.D. thesis, University of Missouri at Columbia, 1996.
 [22] I. Kourbanis, Ph.D. thesis, Northeastern University, 1989.
 [23] D. Allspach *et al.*, in *Advances in Cryogenic Engineering*, edited by R.W. Fast (Plenum, New York, 1991), Vol. 37, p. 1495.
 [24] E. Engels, Jr. *et al.*, Nucl. Instrum. Methods Phys. Res. A **279**, 272 (1989).
 [25] C. Bromberg *et al.*, Nucl. Instrum. Methods Phys. Res. A **307**, 292 (1991).
 [26] These hybrid planes were installed after the commissioning run to provide improved vertex resolution.
 [27] The U, V wires were at angles of 37° and -53° relative to the vertical, respectively.

- [28] F. Lobkowicz *et al.*, Nucl. Instrum. Methods Phys. Res. A **235**, 332 (1985).
- [29] L. Apanasevich *et al.*, Nucl. Instrum. Methods Phys. Res. A **417**, 50 (1998).
- [30] G. Drake *et al.*, Nucl. Instrum. Methods Phys. Res. A **269**, 68 (1988).
- [31] C. Lirakis, in *Proceedings of the First Annual Conference on Electronics for Future Colliders* (Le Croy Corp., Chestnut Ridge, New York, 1991), p. 35.
- [32] C. Benson, M.S. thesis, University of Rochester, 1989.
- [33] A. Gribushin *et al.*, Phys. Rev. D **53**, 4723 (1996).
- [34] A. Gribushin *et al.*, Phys. Rev. D **62**, 012001 (2000).
- [35] V. Koreshev *et al.*, Phys. Rev. Lett. **77**, 4294 (1996).
- [36] R. Jesik *et al.*, Phys. Rev. Lett. **74**, 495 (1995).
- [37] L. Apanasevich *et al.*, Phys. Rev. D **56**, 1391 (1997).
- [38] D.E. Groom *et al.*, Eur. Phys. J. C **15**, 1 (2000).
- [39] L. Sorrell, Ph.D. thesis, Michigan State University, 1995.
- [40] G. Osborne, Ph.D. thesis, University of Rochester, 1996.
- [41] F. Carminati *et al.*, GEANT: Detector Description and Simulation Tool, CERN Program Library Long Writeup W5013, 1993.
- [42] This is in contrast to the analysis of data from the commissioning run where we used just empirical parametrizations of electromagnetic showers in simulating the EMLAC response.
- [43] Fermilab Computing Department, CPS Software User's Guide, FNAL GA0009, 1993.
- [44] G. Marchesini *et al.*, Comput. Phys. Commun. **67**, 465 (1992), HERWIG v5.6.
- [45] T. Sjöstrand, PYTHIA 5.6 and JETSET 7.3 Physics and Manual, CERN-TH.6488/92, 1992.
- [46] M. Bonesini *et al.*, Z. Phys. C **37**, 39 (1987).
- [47] G. Donaldson *et al.*, Phys. Rev. Lett. **40**, 917 (1978).
- [48] G.D. Lafferty and T.R. Wyatt, Nucl. Instrum. Methods Phys. Res. A **355**, 541 (1995).
- [49] X.-N. Wang, Nucl. Phys. **A661**, 609 (1999).
- [50] Private communication with Xin-Nian Wang regarding the use of this program at these beam energies.
- [51] H.L. Lai *et al.*, Phys. Rev. D **55**, 1280 (1997).
- [52] J. Binnewies, B.A. Kniehl, and G. Kramer, Phys. Rev. D **52**, 4947 (1995).
- [53] B.A. Kniehl, G. Kramer, and B. Pötter, Nucl. Phys. **B582**, 514 (2000).
- [54] R.P. Feynman, R.D. Field, and G.C. Fox, Phys. Rev. D **18**, 3320 (1978).
- [55] M. Fontannaz and D. Schiff, Nucl. Phys. **B132**, 457 (1978).
- [56] A.P. Contogouris *et al.*, Nucl. Phys. **B179**, 461 (1981).
- [57] A.P. Contogouris *et al.*, Phys. Rev. D **32**, 1134 (1985).
- [58] J. Collins and D. Soper, Nucl. Phys. **B193**, 381 (1981); **B213**, 545(E) (1983); J. Collins, D. Soper, and G. Sterman, Phys. Lett. **109B**, 388 (1982).
- [59] S. Catani *et al.*, J. High Energy Phys. **03**, 025 (1999).
- [60] S. Catani, M.L. Mangano, and P. Nason, J. High Energy Phys. **07**, 024 (1998).
- [61] H.-L. Lai and H.-N. Li, Phys. Rev. D **58**, 114020 (1998).
- [62] E. Laenen, G. Sterman, and W. Vogelsang, Phys. Rev. Lett. **84**, 4296 (2000).
- [63] N. Kidonakis and J.F. Owens, Phys. Rev. D **61**, 094004 (2000).
- [64] N. Kidonakis and J.F. Owens, Phys. Rev. D **63**, 054019 (2001).
- [65] E. Laenen, G. Oderda, and G. Sterman, Phys. Lett. B **438**, 173 (1998).
- [66] N. Kidonakis, G. Oderda, and G. Sterman, hep-ph/9805279.
- [67] N. Kidonakis, G. Oderda, and G. Sterman, Nucl. Phys. **B525**, 299 (1998).
- [68] C.E. Fink, hep-ph/0105276.
- [69] J.F. Owens, Rev. Mod. Phys. **59**, 465 (1987).
- [70] A.G. Clark *et al.*, Nucl. Phys. **B160**, 397 (1979).
- [71] A.L.S. Angelis *et al.*, Phys. Lett. **97B**, 163 (1980).
- [72] Y. Zhang *et al.*, Phys. Rev. C **65**, 034903 (2002).